Journal of Materials Chemistry A

ROYAL SOCIETY OF CHEMISTRY

PAPER

View Article Online
View Journal | View Issue

Cite this: *J. Mater. Chem. A*, 2026, **14**, 10178

Air stable photo-redox active elusive Cr(III)-tri-dithiolene-radical complexes as a new class of pseudo-supercapacitors with high capacitance: enhancement of energy storage with heavier chalcogenide

Sujit Das,†[a] Mayur Thosare,†[b] Saurav Ghosh,[a] T. Kedara Shivasharma,[b] Subuhan Ahamed,[a] Harsha S. Karnamkkott,[a] Björn Schwarz,*[c] Babasaheb R. Sankapal,*[b] Liviu Ungur[d] and Kartik Chandra Mondal*[a]

Received 15th October 2025
Accepted 21st January 2026

DOI: 10.1039/d5ta08423g

rsc.li/materials-a

Chromium, an earth-abundant metal with an accessible redox potential of −0.74 V *vs.* RHE, emerges as a promising element for the design of high-energy-density supercapacitors. Beyond their intriguing chemistry, energy storage devices employing stable redox-active radicals of main-group elements gain increasing attention for sustainable applications. Herein, the pseudo-supercapacitive properties of two unprecedented, photo-redox active, air-stable Cr(III)-triradical complexes with the general formula [Cr(III)(SS-NHC = E$^{\bullet-}$)$_3$] (**1**, E = S; **2**, E = Se; (SS-NHC = E) : S_2-donor dithiolene ligand) are reported. Electrochemical anodes fabricated by coating these complexes onto stainless-steel substrates exhibited excellent supercapacitance performance. Complex **1** delivered a specific capacitance of 145.2 F g^{-1}, while complex **2** showed a markedly higher value of 340.9 F g^{-1} at 5 mV s^{-1}, centred at $E_{1/2}$ = −0.72 V. Cycling stability reached 81.2% for complex **1** and 87.3% for complex **2** after 3000 cycles. The superior activity of complex **2** arises from the substitution of sulfur with selenium in the SS-NHC = E$^{\bullet-}$ ligand, which enhances redox activity, conductivity, and ion transport. Ragone plot analysis confirmed a higher energy density (14.63 Wh kg^{-1} at 252 W kg^{-1}) for complex **2** compared to complex **1** (8.76 Wh kg^{-1} at 211 W kg^{-1}). Mechanistic studies revealed that complex **1** operated *via* mixed surface- and diffusion-controlled processes, whereas complex **2** predominantly followed diffusion control, enabling efficient charge transport and improved pseudocapacitive behaviour.

1. Introduction

Supercapacitors possess higher energy density than solid-state capacitors and operate at much lower voltage limits, thereby bridging the gap between rechargeable batteries and electrolytic capacitors.[1] Their potential as electrode materials lies in their ability to store energy that is ten to a hundred times greater per unit mass, volume, or surface area than that of electrolytic capacitors.[2] Consequently, supercapacitors have attracted significant research attention from chemists, physicists, material scientists, and engineers, not only for the design and synthesis of new redox-active materials but also for the development of devices for next-generation electronics with shorter charging times and stable voltage outputs.[3] The electrochemical double layer (EDL) supercapacitors store charge *via* double-layer formation at the electrode–electrolyte interface, known as the Helmholtz double-layer, whereas pseudo-supercapacitors store energy through faradaic redox reactions involving charge transfer.[4] Often, these two mechanisms are not entirely separable in their contribution to overall capacitance, with the latter sometimes exhibiting up to an order of magnitude higher energy storage.[5] The power storage capacity of a supercapacitor depends on parameters such as surface area, charge mobility, and the oxidation state of the metal ions, with the combination of the metal and ligand also playing a crucial role.[3,6] Supercapacitors are, in many ways, superior to rechargeable batteries, particularly in terms of power density, rapid charge–discharge capability, and cycling stability; however, they are generally limited by their lower energy density and operating voltage compared to lithium-ion batteries.[7] Nevertheless,

[a]*Department of Chemistry, Indian Institute of Technology Madras, Chennai 600036, India. E-mail: csdkartik@iitm.ac.in*

[b]*Nano Materials and Device Laboratory, Department of Physics, Visvesvaraya National Institute of Technology, Nagpur 440010, Maharashtra, India. E-mail: brsankapal@phy.vnit.ac.in*

[c]*Institute for Applied Materials (IAM), KIT, Hermann-von-Helmholtz-Platz 1, 76344 Eggenstein-Leopoldshafen, Germany*

[d]*Department of Chemistry, National University of Singapore, Office: MD1-05-03A, 119077, Singapore*

† These authors contributed equally to this manuscript.

supercapacitors have already been commercialised in devices ranging from miniature electronic devices to large transport vehicles due to their distinct advantages.[1–7] The global market value of supercapacitors is projected to increase by approximately 24% per year, reaching USD 2 billion by 2026. In this context, it is noteworthy that chromium is the fourth most abundant transition metal in the earth's crust and theoretically exhibits the highest specific capacity (1546 mAh g^{-1}) and volumetric capacity (11 118 mAh cm^{-3}) for a three-electron process at −0.74 V *vs.* the reversible hydrogen electrode.[8] Despite this potential, most studies have focused on chromium oxide phases, nanoparticles, and a limited number of molecular Cr-complexes or composite materials for supercapacitor studies.[9–21] Although extensive research has been conducted on transition-metal oxides and polymeric materials, molecular systems integrating both stable radical character and redox-active metal centres remain largely unexplored for supercapacitor applications. Incorporating metal-radical frameworks offers a unique opportunity to couple electronic delocalisation with reversible charge storage, thereby enabling fast redox-switching and enhanced capacitance. However, isolating such metal-radical complexes that are both air-stable and electrochemically robust has remained an outstanding challenge.

Stable radicals have found widespread use in various areas of chemistry, biology, catalysis, and materials science.[22] Dithiolene ligands [S-(R/Ar)C=C(R/Ar)-S] have attracted considerable attention since the 1960s due to their role as redox non-innocent cofactors in metalloproteins, acting as a two-sulfur-donor chelating ligand (Fig. 1a).[23,24] A distinctive feature of such dithiolene ligands is their ability to adopt different electronic states-singlet dianion, doublet mono-anionic radical, and neutral singlet depending on the electrochemical potential [$L^{2-} \rightarrow L^{\bullet-} \rightarrow L^{0}$] (Fig. 1b).[22–24] The metal-dithiolene-radical intermediates are the most intriguing species in biological systems, which are quite challenging to isolate for characterisation.[23,24] In 2017, Robinson and co-workers reported a chemically distinct and captivating route to the synthesis of an *N*-hetero cyclic carbene-based dithiolene radical anion, which they successfully isolated as its crystalline lithium salt [$(THF)_2$Li(SS-NHC = S)] (Fig. 1; bottom, right).[25] They extensively investigated its redox properties and chemical reactivities towards main group elements such as Si and Ge, producing diamagnetic compounds, while chemical species of B and Al, retaining the radical character, have been isolated and characterised.[26] The isolation of a neutral aluminum(III)-triradical complex containing an octahedral Al(III) ion was quite remarkable.[26b] Robinson's group also summarized[26b] synthetic efforts of octahedral Cr(III)-diradical and Cr(III)-triradical complexes by Karl Wieghardt *et al.*[27–30] Robinson *et al.* clearly stated that the isolation of Cr(III)-triradical complexes of the dithiolene ligand[27,28] by Karl Wieghardt *et al.* was unsuccessful. Hence, the isolation of the octahedral Al-triradical complex of the dithiolene radical was unique.[26b]

This study establishes a new design paradigm for molecular supercapacitors, demonstrating the first direct link between

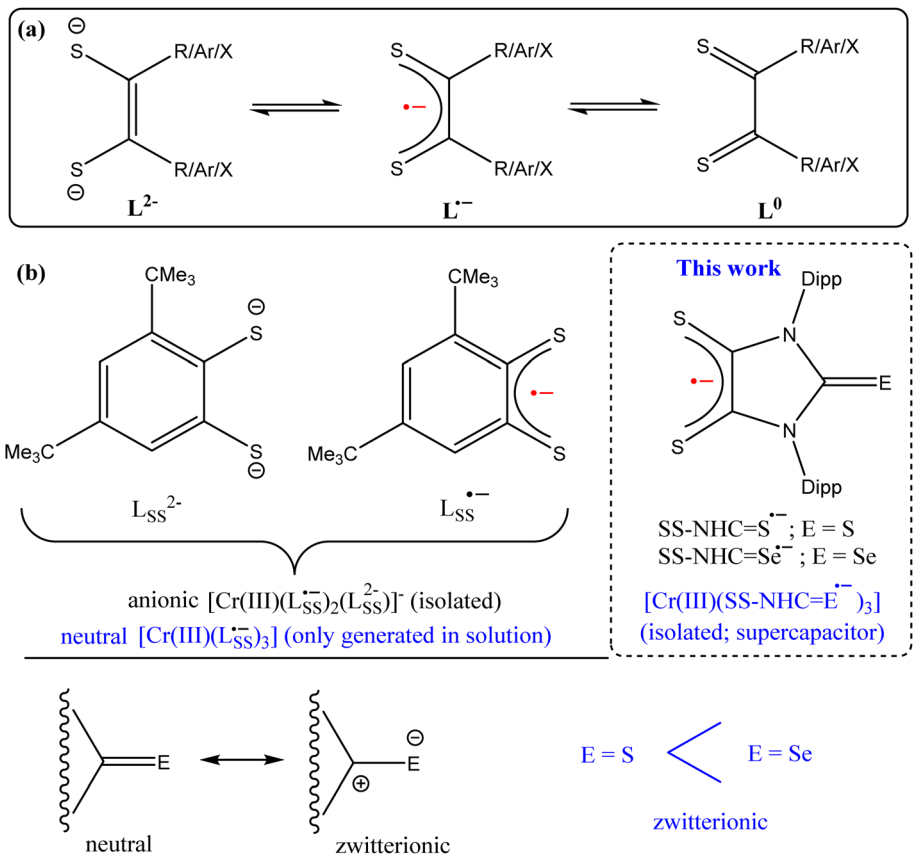

Fig. 1 Redox states of dithiolene ligands (a) and Cr(III)-dithiolene complexes (b).

metal-radical redox chemistry and electrochemical energy storage. Herein, we report the first air-stable, redox-active Cr(III)-triradical complexes that exhibit pseudo-supercapacitive behaviour. These complexes uniquely combine a high-spin Cr(III) centre with three ligand-based radicals, creating a molecular architecture capable of rapid and reversible multi-electron redox processes. This approach introduces a new molecular framework for supercapacitor electrode design based on discrete metal-radical complexes rather than conventional metal oxides or polymeric materials. Building on the pioneering work of Robinson and Wieghardt on dithiolene radical chemistry, we extended this concept to chromium complexes, successfully isolating two unprecedented triradical species, $[Cr(III)(SS\text{-}NHC = E^{\bullet -})_3]$ (**1**, E = S; **2**, E = Se; Scheme 1) and demonstrating their electrode performance. Notably, the substitution of sulfur by selenium significantly enhances energy storage and cycle stability, attributed to the increased polarity of the C=Se bond (Fig. 1c).

2. Results and discussion

Karl Wieghardt *et al.* synthesized the violet colored anionic Cr-diradical complex $[Cr(III)(L_{SS}^{\bullet -})_2(L_{SS}^{2-})]^-$ by reacting anhydrous $CrCl_3$ with the H_2L_{SS} ligand in the presence of triethylamine as a base.[27,28] The lithium salt of the *N*-hetero cyclic carbene (NHC) functionalized dithiolene radical anion $[Li(THF)_2SS\text{-}NHC = E]$ [E = S, Se] was reacted with anhydrous $CrCl_2$ in THF for 16 h at RT to obtain a dark green solution of the Cr(III)-triradical complex $[Cr(III)(SS\text{-}NHC = E^{\bullet -})_3]$ (E = S, complex **1**; E = Se, complex **2**) (Scheme 1). Dark green rods of complexes **1** and **2** were grown from *n*-hexane solution at rt in 55% to 60% yield. The powders of complexes **1** and **2** are stable till 150 °C. Single crystals of complexes **1–2** are stable in open air for at least one day, which has been concluded from UV-vis measurements (see Fig. S2 and S3). Single crystals of complexes **1–2** take nearly two weeks for the decomposition of 25% (complex **1**) to 50% (complex **2**) in the solid state. The formation of the mono-anionic complex $[Cr(III)(SS\text{-}NHC = E^{\bullet -})_2(SS\text{-}NHC = E^{2-})]^-$ (E = S, $\mathbf{1}^-$; E = Se, $\mathbf{2}^-$) (Scheme 1) is expected when three equivalents of mono-anionic dithiolene radical ligand $SS\text{-}NHC = E^{\bullet -}$ react with $Cr(II)Cl_2$ with the elimination of two equivalents of LiCl. The neutral Cr(III)-triradical complex $[Cr(III)(SS\text{-}NHC = E^{\bullet -})_3]$ is formed *via* a redox reaction between $[Cr(III)(SS\text{-}NHC = E^{\bullet -})_2(SS\text{-}NHC = E^{2-})]^-$ and another equivalent radical ligand $SS\text{-}NHC = E^{\bullet -}$, forming the dianionic dithiolene ligand $SS\text{-}NHC = E^{2-}$. The monoanionic Cr-complex $[Cr(III)(SS\text{-}NHC = E^{\bullet -})_2(SS\text{-}NHC = E^{2-})]^-$ was isolated as green rods in the presence of a bulky cation, $(Ph_3P)_2CH^+$ (Scheme 1), in low yield. Alternatively,

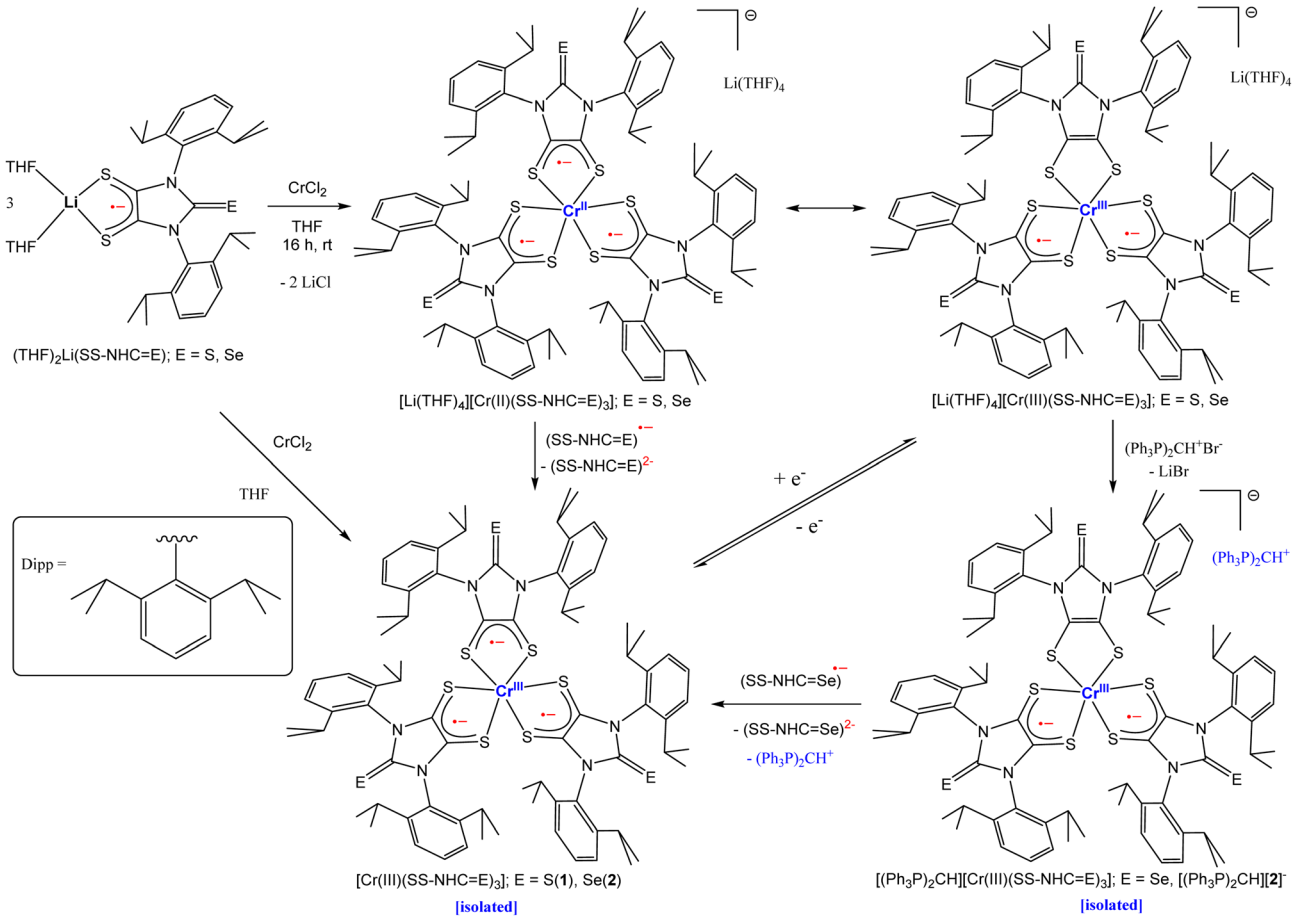

Scheme 1 Synthesis of neutral and anionic forms of Cr(III)-triradical complexes $[Cr(III)(SS\text{-}NHC = E^{\bullet -})_3]$ [complex **1**, E = S; complex **2**, E = Se] and $[Cr(III)(SS\text{-}NHC = E^{\bullet -})_2(SS\text{-}NHC = E^{2-})_3]^-$ $(\mathbf{1–2})^-$.

$[Cr(III)(SS\text{-}NHC = E^{\bullet -})_2(SS\text{-}NHC = E^{2-})]^-$ was generated in solution *via* potassium graphite (KC_8) reduction of its neutral analogue $[Cr(III)(SS\text{-}NHC = E^{\bullet -})_3]$ (Scheme 1). Potassium graphite (KC_8) is a strong, heterogeneous reducing agent.

Complexes **1** and **2** are isomorphous; therefore, only the structural features of complex **2** are described here. The structure of complex **1** is detailed in Section 9 of the SI (Single Crystal X-ray Diffraction section). Complex **2** crystallises in the monoclinic *C*2/*c* space group. The molecular structure of complex **2** contains three anionic radical ligands, SS-NHC = $Se^{\bullet -}$, and one Cr(III) ion ($3d^3$), which adopts a distorted octahedral geometry with an S_6 donor set. The S–Cr–S angle with each chelating S_2-donor ligand is nearly 90° while the angle between the two axes of opposite Cr–S bonds is nearly 171°.[27,28] The corresponding angles are ~83–84° and ~159–164° for the previously reported anionic $[Cr(III)(L_{SS}^{\bullet -})_2(L_{SS}^{2-})]^-$ complex. The Cr–S bond distances fall in the range of 2.3644(7)–2.3950(7) Å for **1** and 1.386(3)–1.393(3) Å for **2**, which are significantly longer than those of $[Cr(III)(L_{SS}^{\bullet -})_2(L_{SS}^{2-})]^-$ (2.28–2.32 Å).[27,28] The C–C bond distances, for each of the imidazole rings, are in the range of 1.394(6)–1.401(6) Å for **1** and 1.386(3)–1.393(3) Å for **2**, which is similar to that reported in our very recently reported $[Fe(III)(SS\text{-}NHC = Se^{\bullet -})_3]$ complex[39b] and other metal radical complexes.[25,26]

The X-ray photoelectron spectroscopy (XPS) measurement of complex **1** showed two bands at 575.6 eV and 583.7 eV, for the $2p_{3/2}$ and $2p_{1/2}$ states, corresponding to the Cr^{3+} ion ($3d^3$, S = 3/2) in the system. These values are consistent with the literature values of binding energies of $2p_{3/2}$ and $2p_{1/2}$ in the range of 575–578 and 584–586 eV, respectively.[8] The DC magnetic susceptibility measurements were carried out on ground single crystals of complexes **1–2** in the temperature range of 2–300 K (Fig. 3). The possible spin states are $S_T = |3/2–3/2|$ to $|3/2 + 3/2| = 0$ to 3 (0, 1, 2, and 3) for the Cr(III) ion [$3d^3$; $g \approx 2$] coupling with three unpaired electrons on ligands [S_T = spin state of the complex]. The experimental value of the χ_T product of complexes **1–2** below 0.15 cm^3 K mol^{-1} suggests that a very small percentage of triplet (S = 1) states of complexes **1–2** is populated, while singlet diamagnetic forms (S = 0) are mainly present. This is also reflected in the *M vs.* H plot (Fig. 3, inset). The spin ground state of complexes **1–2** is a singlet, which was also previously reported for octahedral Cr(III)-triradical complexes of N_2- and O_2-donor anionic radical ligands [$L_{NN}^{\bullet -}$ and $L_{OO}^{\bullet -}$].[29,30] EPR spectra in the solid-state are shown in the SI.

The weak vibrational Raman bands of complex **1** at 90 and 146 cm^{-1} are attributed to lattice vibrations, which typically appear in the 50–200 cm^{-1} region.[31] A sharp band at 219 cm^{-1} is assigned to asymmetric Cr–S stretching modes, consistent with prior studies.[32–35] Additional peaks at 425 cm^{-1} are also linked to Cr–S stretching vibrations (Fig. 4, left) of complex **1**, which match well with known vibrational frequencies of metal–sulphur bonds.[33,34,36] Furthermore, a sharp band at 475 cm^{-1} is attributed to N–C–S deformation vibrations of complex **1**, typically occurring between 400 and 500 cm^{-1}.[37] The band at 854 cm^{-1} was assigned to C–C stretching mode. The medium-intensity band observed at 972 cm^{-1} of complex **1** is assigned to C_3N_2 aromatic ring deformation modes, typically occurring in the 980–1100 cm^{-1} range.[31] The sharp bands at 1170–1246 cm^{-1} are most like due to the vibrational Raman bands for C–C/C–N bonds. The symmetric normal mode at 1505 cm^{-1} can be attributed to the C=N bond.[33b] A weak band at 1591 cm^{-1} may be due to the vibrational Raman band for the C=C bond. Very similar bands were observed for the Se-analogue (complex **2**) (Fig. 4, right). Further weak bands at around 600 and 765 cm^{-1}

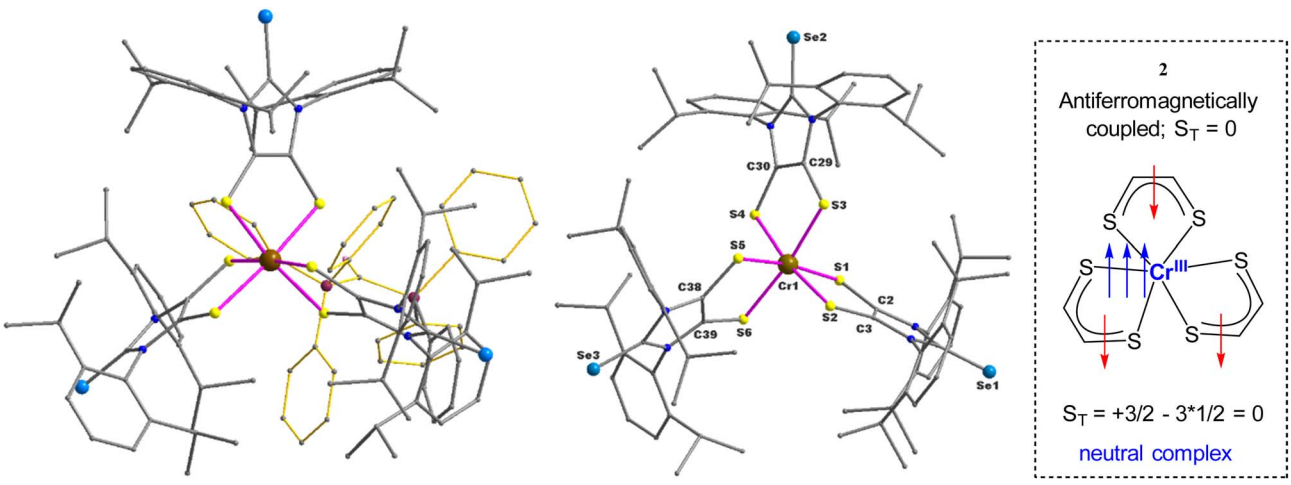

Fig. 2 Molecular structures of the anionic (left; complex 2^-) and neutral Cr(III)-complex [Cr(III)(SS-NHC = Se)$_3$] (complex **2**) [E = Se; left]. The counter cation $[(Ph_3P)_2CH^+]$ of 2^- is shown in a light yellow colour. All the H-atoms were omitted for clarity. Bond parameters of complex **2** [Å]: Cr(1)–S(1) 2.3950(7), Cr(1)–S(2) 2.3704(7), Cr(1)–S(3) 2.3644(7), Cr(1)–S(4) 2.3914(7), Cr(1)–S(5) 2.3803(7), Cr(1)–S(6) 2.3735(7); S(2)–Cr(1)–S(1) 89.29(2), S(3)–Cr(1)–S(4) 89.45(2), S(6)–Cr(1)–S(5) 89.44(2), S(3)–Cr(1)–S(6) 172.64(3), S(2)–Cr(1)–S(4) 171.31(3), S(5)–Cr(1)–S(1) 171.88(3). See Tables S1–S3 and Section 9 of the SI (Single Crystal X-ray Diffraction section) for details on bond parameters of complex **1**. Spin structure of complexes **1–2** showing $S_T = 0$ ground state (right), concluded from DC magnetic susceptibility measurements. Three blue colored arrows represent the spins on the central octahedral Cr(III) ion, while each red colored arrow represents the spin of each radical of the SS-NHC = E ligand.

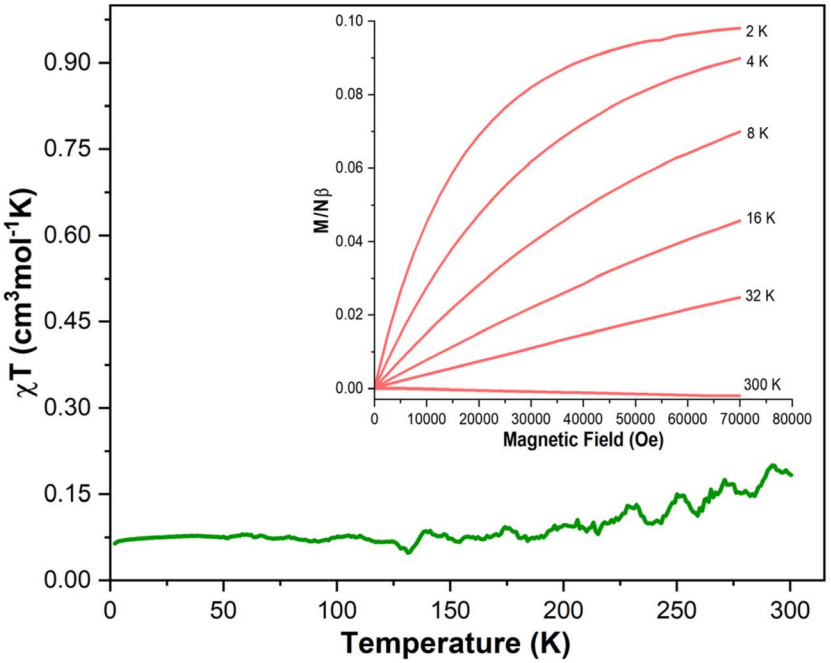

Fig. 3 Plots of χ_T *vs.* *T* (green line) and M *vs.* H (red line, inset) for the complexes [Cr(III)(SS-NHC = Se)$_3$], [E = Se (complex **2**)]. See Fig. S20 (in the SI) for complex **1**.

reflect the C–Se stretching vibrations, commonly found within the 570–750 cm^{-1} region.[33,37,38]

Very recently, well-known [M(dithiolene)$_2$]$^{n-}$ [M, Cu, Ni; n = 2, 3] complexes were further studied by resonant sulfur Kβ ($1s^3p$) X-ray emission spectroscopy (XES) and resonant inelastic X-ray scattering (RIXS) to obtain valence excited states and the core–valence couplings of the complexes.[39a] The authors strongly expressed their major concern about the effect of highly covalent metal bonding interactions, making it challenging for the formal assignment of metal and ligand redox states unambiguously.[39a] EDA-NOCV analyses of [Cr(III)(^{Me}SS-NHC = Se$^{\bullet-}$)$_3$] (**2′**) were carried out to get a deeper insight into bonding, pair-wise spin–spin interaction energy, degree of covalent characters, and distribution of electron densities between chromium and the dithiolene ligand (Fig. 5). Dipp groups in complexes **1–2** were replaced by Me groups in **1′–2′** for simplicity of density functional theory (DFT) calculation. The estimation of covalent character during interactions between the Cr(III) ion and SS-NHC = Se$^{\bullet-}$ will be most crucial since it is challenging to explain the preference for the singlet spin ground state of the Cr(III)-triradical complex (Table S8 and Fig. S32).

The model Cr(III)-triradical complex [Cr(III)(^{Me}SS-NHC = Se$^{\bullet-}$)$_3$] (**2′**) was optimized in the singlet spin ground state and split into two fragments as [Cr(III)(^{Me}SS-NHC = Se$^{\bullet-}$)$_2$]$^+$ and [(^{Me}SS-NHC = Se$^{\bullet-}$)]$^-$ in the cationic doublet (D) and anionic doublet (D) respectively for EDA-NOCV calculations breaking two Cr–S bonds (Fig. 5). The analyses showed that the bonding interaction energy of a pair of Cr–S bonds is nearly −180 kcal mol^{-1}, with contributions due to electrostatic and covalent interaction energies of 54.3% and 41.3% respectively. The pair-wise stabilisation energy for the interaction between singly occupied molecular orbitals (SOMOs) of [Cr(III)(^{Me}SS-NHC = Se$^{\bullet-}$)$_2$]$^+$ and [(^{Me}SS-NHC = Se$^{\bullet-}$)]$^-$ fragments with opposite spins was quantified to be nearly $\Delta E_{orb(1)}$ = −31.2 kcal mol^{-1}, which is nearly 20% of the total covalent interaction energy (ΔE_{orb}) for a covalent π-bond.

Two other dative-type stronger bonding interactions of −40.4 and 46.7 kcal mol^{-1} [Cr(III) ← SS-NHC = Se] from a non-bonded electron pair on s-atoms were also identified (See Section 13 of the SI for details). Such an analysis of previously reported Cr-dithiolene complexes has not been reported yet.[27,28] These results were compared with those of a very recently reported Fe(III)-triradical complex with a low-spin Fe(III) ion.[39b] The total interaction energy and covalent interaction energy are significantly higher for the Cr-analogue (complex **2**), explaining the stronger antiferromagnetic interaction in this series of complexes. We also have carried out EDA-NOCV analyses for (**2′**)$^{\bullet-}$, keeping in mind previous reports on isolation and characterisation of the anionic doublet complex [Cr(III)($L_{SS}^{\bullet-}$)$_2$(L_{SS}^{2-})]$^-$.[27,28] The EDA-NOCV results showed that the interaction energy between Cr(III) and one of the radical anions drops by nearly 66 kcal mol^{-1}, which may be due to the presence of another ligand dianionic state. The covalency in Cr–S bonds of (**2′**)$^{\bullet-}$ remains nearly the same as in neutral **2′**, with a significant decrease in ionic character by nearly 6% in the anionic doublet state (**2′**)$^{\bullet-}$ (Fig. S33 and Table S9).

DFT calculations at the anionic doublet state (S = $\frac{1}{2}$) of (**1′–2′**)$^{\bullet-}$ showed that major spin densities [α (3.286) and β (2.287) spin densities] are mainly on Cr-centres, which is also reflected in their EPR spectra (Fig. 6). Three unpaired electrons (α) are accumulated at the central Cr(III) ion while two unpaired electrons (β) are delocalized among the three SS-NHC = E ligands of (**1′–2′**)$^{\bullet-}$ ([Cr(III)(SS-NHC = E$^{\bullet-}$)$_2$(SS-NHC = E^{2-})]$^-$). They are

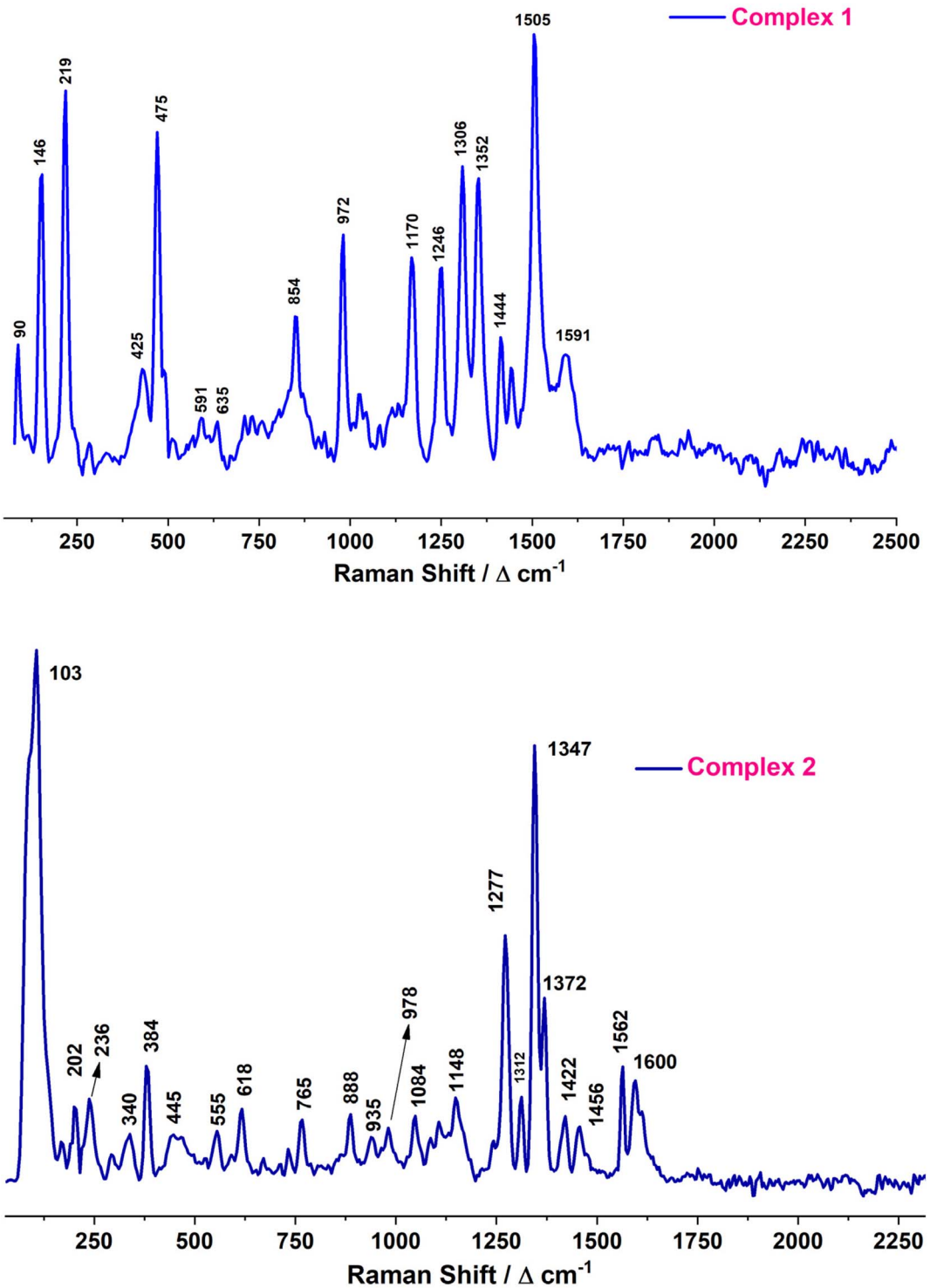

Fig. 4 Solid state Raman spectra of Cr(III)-triradical complexes [Cr(III)(SS-NHC = E$^{\bullet-}$)$_3$] [complex **1**, E = S (left); complex **2**, E = Se (right)] measured using an alpha300 R Raman microscope with a 532 nm laser.

oppositely oriented. The characteristic four satellites are due to the ^{53}Cr nucleus ($I = -3/2$; 9.5% ^{53}Cr) with a coupling constant of 65–67 MHz (see caption of Fig. 6). The dark green plates of **2**$^{\bullet-}$ were isolated in the presence of a suitable cation and characterized by X-ray single crystal diffraction (Fig. 2, left).

Complexes [Cr(III)(SS-NHC = E$^{\bullet-}$)$_3$] (**1**–**2**) were further studied by cyclic voltammetry (CV) measurements, showing multiple redox processes in the potential range from −0.2 to −2.2 V (Fig. 7). The first/second reductions take place near $E_{1/2}$ = −0.51/-1.11 V (complex **1**) and −0.33/-0.72 V (complex **2**), corresponding to a one-electronic process in THF solution [(**1**/**2**)

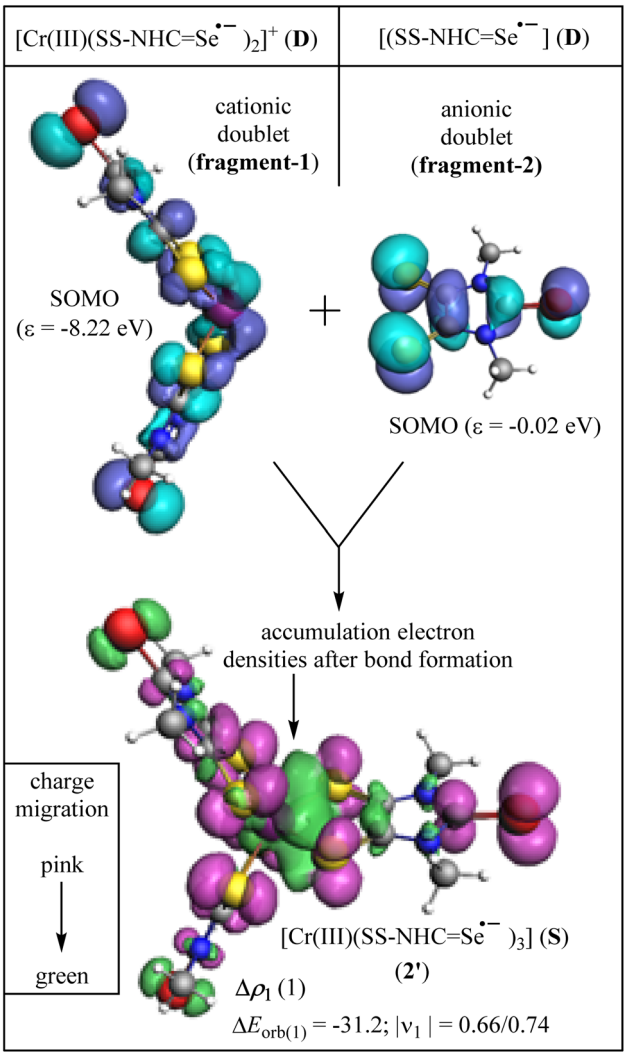

Fig. 5 The shape of the deformation densities $\Delta\rho_{(1)}$ of complex **2′** (S) [$S = 0$] with charged $[CrL_2]^+$ (D) and SS-NHC = $Se^{\bullet-}$ (D) in doublet states at the B3LYP-D3(BJ)/TZ2P level with an iso-surface value of 0.001 au. The eigenvalues $|\nu_1|$ give the size of the charge migration in e. The charge flow direction of the deformation densities is from pink → green; the half-filled orbitals (SOMO) are represented by the lavender and cyan colour combination. Dipp groups in complexes **1–2** were replaced by Me groups in **1′–2′** for simplicity of density functional theory (DFT) calculation.

$+ e^- \rightarrow (\mathbf{1/2})^{\bullet-} + e^- \rightarrow (\mathbf{1/2})^{2-}$] ([Cr(III)(SS-NHC = $E^{\bullet-}$)$_3$] → [Cr(III)(SS-NHC = $E^{\bullet-}$)$_2$(SS-NHC = E^{2-})]$^-$ → [Cr(III)(SS-NHC = $S^{\bullet-}$)(SS-NHC = E^{2-})$_2$]$^{2-}$).[27,28] The electron affinity values of **1′–2′** are computed to be favourable by 101.5 and 105.4 kcal mol^{-1}, respectively, at the B3LYP-D3(BJ)/def2-TZVPP level of theory. Complexes **1–2** were treated with one equivalent of KC_8 in THF, leading to a change in colours. The resultant reaction solutions were also studied by UV-vis and EPR measurements. The Cr(III)-radical complexes with octahedral Cr(III) ions chelated by three sets of O_2- and N_2-donor anionic radical ligands were well studied *via* spectroscopic characterisation and theoretical calculations by Karl Wieghardt *et al.*[29,30]

There is a noticeable change in colour of the THF solution upon treatment with KC_8 (blue to purple for complex **1**; sky-green to bright green for complex **2**; Fig. 8 and 9), which was reflected in EPR spectra. The hyperfine lines due to the coupling with ^{14}N nuclei were visible with a coupling constant of 5.11 MHz ($\mathbf{1}^{\bullet-}$) at $g \approx 2$ (Fig. 10, left) since the abundance of ^{14}N nucleus (99.6%; $I = 1$) is much higher than ^{53}Cr (9.5%; $I = -3/2$). The shape of the EPR spectrum of $\mathbf{2}^{\bullet-}$ is due to an axial nature with a ^{14}N coupling constant of 5.37 MHz near $g \approx 2$.[27] The electron transfer reduction could occur either at the Cr-site [Cr(III) → Cr(II)] or at one ligand centre [$(\mathbf{L})^{\bullet-} \rightarrow (\mathbf{L})^{2-}$]. The distribution of Mulliken spin densities at the anionic doublet state of complexes **1–2** showed that the externally added electron mostly resides on one of the three dithiolene radical ligands, leading to the formation of a SS-NHC = E^{2-} [$\mathbf{1/2} + e^- \rightarrow (\mathbf{1/2})^{\bullet-}$] (Fig. 8). This means that KC_8 mediated reduction is ligand-centre rather than Cr-centre; [Cr(III)(SS-NHC = E^{2-})(SS-NHC = $E^{\bullet-}$)$_2$]$^-$ ($\mathbf{1}^{\bullet-}$, E = S) ($\mathbf{2}^{\bullet-}$, E = Se).

UV-vis measurements showed that complexes [Cr(III)(SS-NHC = $S^{\bullet-}$)(SS-NHC = E^{2-})$_2$]$^{2-}$ $(\mathbf{1/2})^{2-}$ absorb at 900/950, 652/723, and 522 nm in THF. The colour of previously isolated anionic [Cr(III)($L_{SS}^{\bullet-}$)$_2$(L_{SS}^{2-})]$^-$ was reported to be violet.[27,28] [Cr(III)(SS-NHC = $S^{\bullet-}$)$_3$]$^-$ ($\mathbf{1} \rightarrow \mathbf{1}^{2-}$; E = S) was reported to be dark green in color. The UV-vis bands of complex **1** at 900, 652, and 522 nm were shifted to 792, 624, and 535 nm, corresponding to the formation of anionic species ($\mathbf{1}^{2-}$) (Fig. 8, top, left). A similar trend was previously reported for Cr-dithiolene complexes.[27,28] A broad NIR band in the range of 1200–2000 nm disappears on oxidation of anionic [Cr(III)($L_{SS}^{\bullet-}$)$_2$(L_{SS}^{2-})]$^{2-}$ to the neutral [Cr(III)($L_{SS}^{\bullet-}$)$_3$] complex with two stronger bands at ~600 nm.[27] The computed Mulliken spin densities of $(\mathbf{1}')^{2-}$ at the triplet state are shown in Fig. 9. The shifting of UV-vis bands at 950 and 723 nm (**2**) to 914 and 660 nm ($\mathbf{2}^{2-}$) was observed (Fig. 8, top, right). These two redox-active neutral complexes were next utilised as an electrode, and their supercapacitor properties were studied.

2.1 Electrode preparation of complex 1 and complex 2

Dark-coloured redox-active complexes, complex-**1** and complex-**2**, were coated onto polished stainless steel (SS) substrates using a cost-effective doctor-blade technique. The electrode slurry was prepared by homogeneously dispersing 80 wt% of the respective Cr complex with 10 wt% polyvinylidene fluoride (PVDF) and 10 wt% carbon black in *N*-methyl-2-pyrrolidone (NMP), forming a uniform, viscous paste. This slurry was then uniformly applied onto the SS substrates using a blade applicator. The coated films were subsequently dried at 80 °C under ambient conditions overnight to produce electrodes suitable for electrochemical characterization. The mass loading of the complex **1** and **2** electrodes was determined by weighing the substrate before and after coating, yielding an average value of approximately 1.1 mg cm^{-2} over an active area of 1 cm × 1 cm.

3. Supercapacitance studies

The electrochemical characteristics of complex-**1** and complex-**2** electrodes were investigated using a conventional three-electrode configuration, employing platinum (Pt) as the

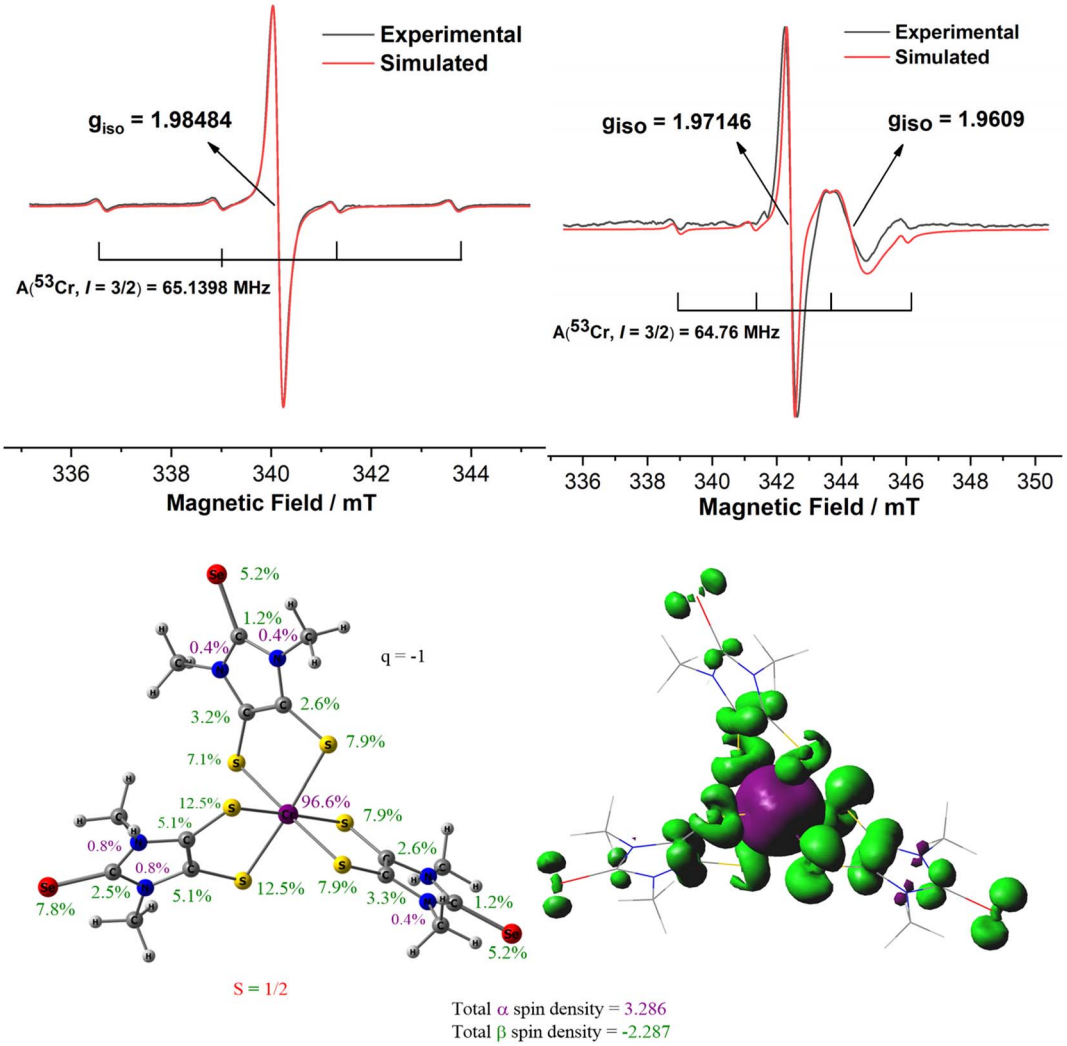

Fig. 6 X-band EPR spectrum (black) of the complexes $\mathbf{1}^{\bullet-}$ (left) and $\mathbf{2}^{\bullet-}$ (right) at rt in THF solution (top) generated *via* KC_8 reduction of complexes **1** and **2**, respectively. Red and black lines represent the simulated and experimental spectra, respectively. Simulation with the EasySpin program,[40] for complex **1**: [g_{iso} = 1.98484, LWPP (Gaussian broadening) = 0.105484 mT, LWPP (Lorentzian broadening) = 0.155 mT, A(^{53}Cr, 9.501%) = 65.1 MHz, X-band experimental frequency = 9.4492 GHz]. For complex **2**: [higher intensity signal at g_{iso} = 1.97146, LWPP (Gaussian broadening) = 0.156 mT, LWPP (Lorentzian broadening) = 0.16 mT, A(^{53}Cr) = 64.76 MHz; lower intensity signal at g_{iso} = 1.9609, LWPP (Gaussian broadening) = 0.493 mT, LWPP (Lorentzian broadening) = 0.80 mT, X-band experimental frequency = 9.448758 GHz]. The Mulliken spin densities of anionic complex $\mathbf{2}^{\bullet-}$ ($q = -1$, $S = 1/2$) calculated at the B3LYP-D3(BJ)/def2-TZVPP level of theory. The percentages of α (3.286) and β (2.287) spin densities are represented on the left side, and the spin density plot is given on the right side. (Purple colour indicates α spin density and green colour denotes the beta spin density).

counter electrode, Ag $AgCl^{-1}$ as the reference electrode, and Cr-based thin films as the working electrodes. Electrochemical measurements were conducted in 1 M LiCl aqueous electrolyte across a potential window ranging from −0.2 to −0.9 V. The areal capacitance was determined from the CV curves using a standard calculation method to assess the charge storage performance of the electrodes.

$$C = \frac{\int I \, dV}{\Delta V \times A \times v} \times 1000$$

where 'C' is the areal capacitance (mF cm^{-2}), '$\int I \, dV$' is the integral of current over voltage, 'ΔV' is the voltage window (V), 'A' is the electrode area (cm^2), and 'v' is the scan rate (mV s^{-1}). Areal capacitance of the electrode material was calculated from these GCD curves using the formula:

$$C_{GCD} = \frac{I_\rho \, \Delta t}{\Delta V}$$

where 'I_ρ' is the current density, 'Δt' is the discharging time, and 'ΔV' is the potential window in volts.

It is worth mentioning that S and Se containing radicals are experimentally reported to be more conducting, and hence, we envisioned that they could be advantageous for supercapacitor properties.[41] Imidazolium salt was also shown to be a potential electrode for supercapacitor studies.[42] Thus, the imidazolium ring, functionalized with three chalcogenide atoms [SS-NHC = E; E = S, Se], may inherently possess the aspect of

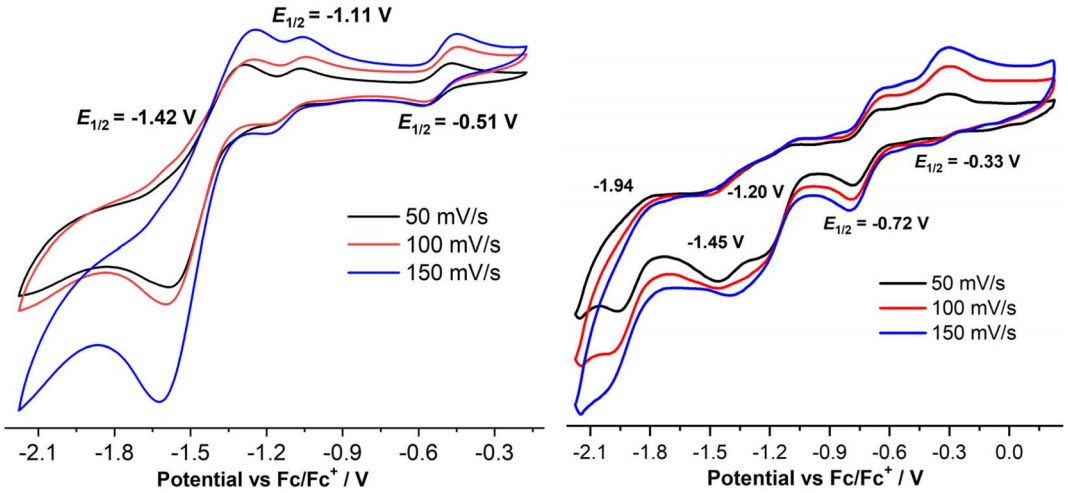

Fig. 7 The cyclic voltammogram of complexes Cr(III)(SS-NHC = E)$_3$], [E = S (complex **1**) (left); E = Se (complex **2**) (right)] in THF at rt containing 0.1 M [*n*-Bu$_4$N][PF$_6$] as supporting electrolyte, at scan rates of 50/100/150 mV s^{-1}. Glassy carbon was used as the WE (working electrode), platinum wire as the CE (counter electrode) and Ag wire as the RE (reference electrode).

supercapacitor properties. Thus, redox-active Cr(III)-triradical complexes **1–2** were coated on stainless steel to prepare anodes to explore supercapacitor properties.[8–21] The cyclic-voltammogram (CV) profiles of complexes **1** (Fig. 11(a) inset) and **2** (Fig. 11(b) inset) based on electrodes in 1 M LiCl displayed quasi-rectangular shapes with mild redox features, indicating a combination of electric double-layer capacitance (EDLC) and pseudocapacitive behaviour.[43–45] This hybrid charge storage mechanism involves both electrostatic ion accumulation at the electrode–electrolyte interface and fast, reversible surface or

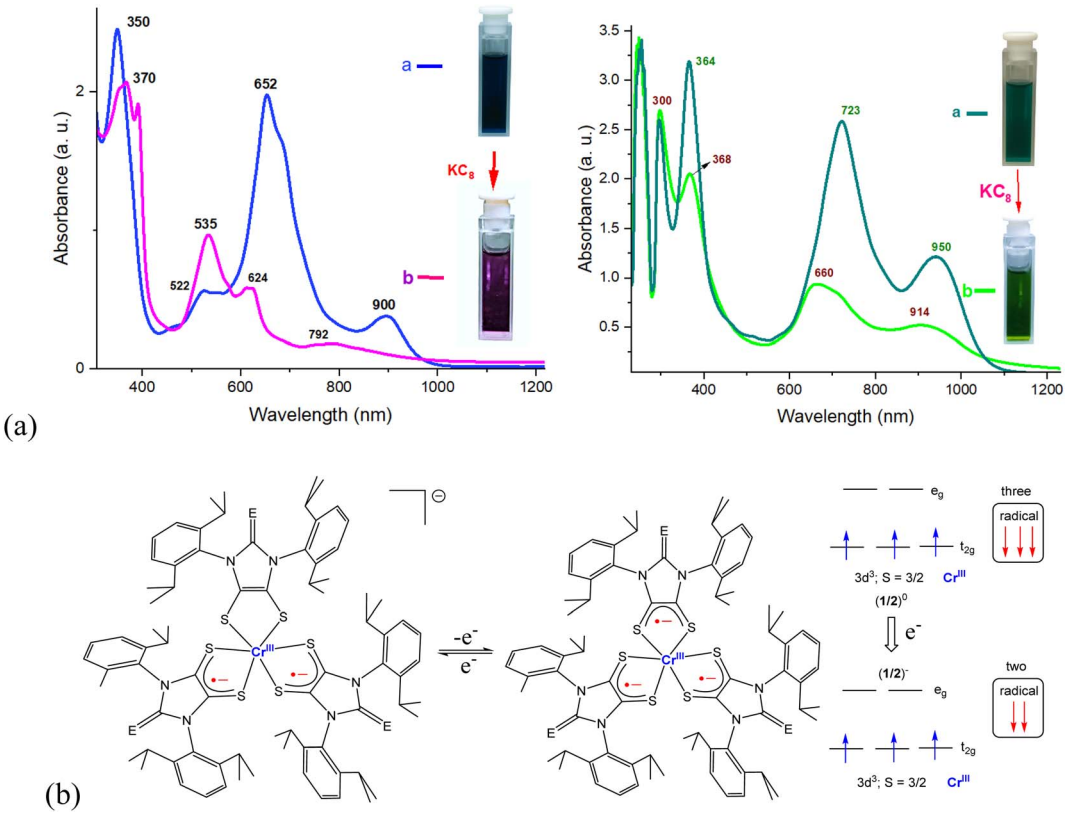

Fig. 8 (a) (Top) UV-vis spectrum of complexes [Cr(III)(SS-NHC = S)$_3$] (complex **1**) (left) and [Cr(III)(SS-NHC = Se)$_3$] (complex **2**) (right) in THF solution. (b) UV-vis spectrum of the two-electron-reduced species generated *in situ* by reaction with two equiv. KC$_8$ in THF at 350, 652, 522, and 900 (nm) (complex **1**). (Bottom) Anionic and neutral complexes and their spin structures.

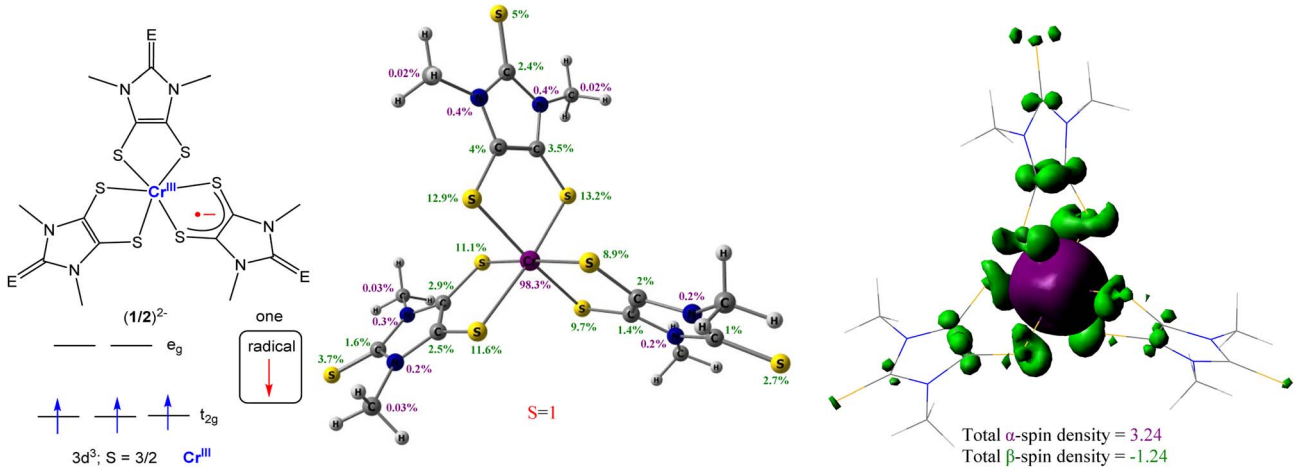

Fig. 9 The Mulliken spin densities of the dianionic complex [Cr(III)(SS-NHC = S$^{\bullet-}$)(SS-NHC = S^{2-})$_2$]$^{2-}$ (**1′**)$^{2-}$ (S = 1) calculated at the B3LYP-D3(BJ)/def2-TZVPP level of theory [α-spin densities 3.24 (purple) and β-spin densities 1.24 (green)]. The α spin density percentage is represented on the left side, and the spin density plot is given on the right side. (Purple colour indicates α spin density and green colour denotes the beta spin density). Dipp groups of **1**$^{2-}$ were replaced by Me (**1′**)$^{2-}$ on N-atoms.

near-surface redox reactions.[46–49] Fig. 11(a) and (b) depict the variation of areal and specific capacitance with scan rates for complexes **1** and **2**, respectively.

At a scan rate of 100 mV s^{-1}, the specific capacitance values for complexes **1** and **2** were calculated to be 40.7 and 87.1 F g^{-1}, respectively (with corresponding areal capacitances of 44.8 and 95.7 mF cm^{-2}, respectively). As the scan rate decreased, improved ion diffusion allowed greater access to active sites, enhancing the capacitive response.[50–52] Complexes **1** and **2** exhibited maximum specific capacitances of 145.2 and 320.2 F g^{-1}, respectively, when measured at a scan rate of 5 mV s^{-1} (with areal capacitances of 159.8 and 352.2 mF cm^{-2}, respectively). The more significant increase in capacitance at lower scan rates for complex **2** suggests a dominant diffusion-

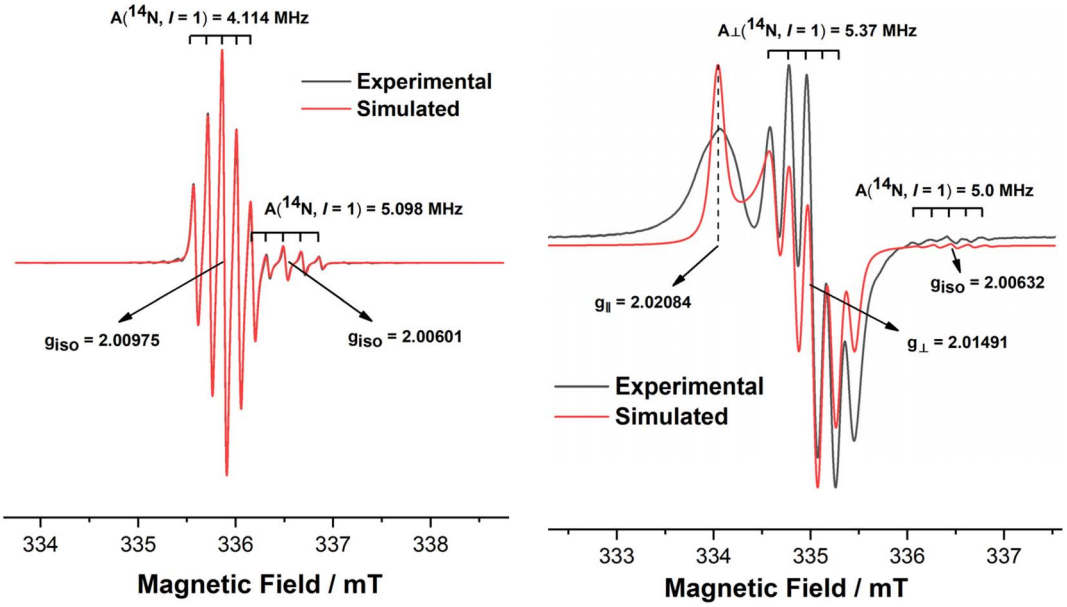

Fig. 10 X-band EPR spectrum (black) of complexes **1**$^{2-}$ (left) and **2**$^{2-}$ (right) after the reaction with KC_8 at rt in THF. Red and black lines represent the simulated and experimental spectra, respectively, and the simulation is done using the EasySpin program.[40] [Two signals – #1: more intense signal → g_{iso} = 2.00975, LWPP (Gaussian broadening) = 0.027 mT, LWPP (Lorentzian broadening) = 0.034 mT, A(^{14}N) = 4.1 MHz; #2: Less intense signal → g_{iso} = 2.00601, LWPP (Gaussian broadening) = 0.0400014 mT, LWPP (Lorentzian broadening) = 0.016 mT, A(^{14}N) = 5.1 MHz, X-band experimental frequency = 9.4481 GHz]. For **2**: [two signals – #1: more intense signal → $g_{\|}$ = 2.02084, $g_{\perp}$ = 2.01491, LWPP (Gaussian broadening) = 0.074055 mT, LWPP (Lorentzian broadening) = 0.059 mT, $A_{\perp}$ (^{14}N) = 5.4 MHz; #2: less intense signal → g_{iso} = 2.00632, LWPP (Gaussian broadening) = 0.0421275 mT, LWPP (Lorentzian broadening) = 0.047 mT, A(^{14}N) = 5.0 MHz; X-band experimental frequency = 9.4487 GHz].

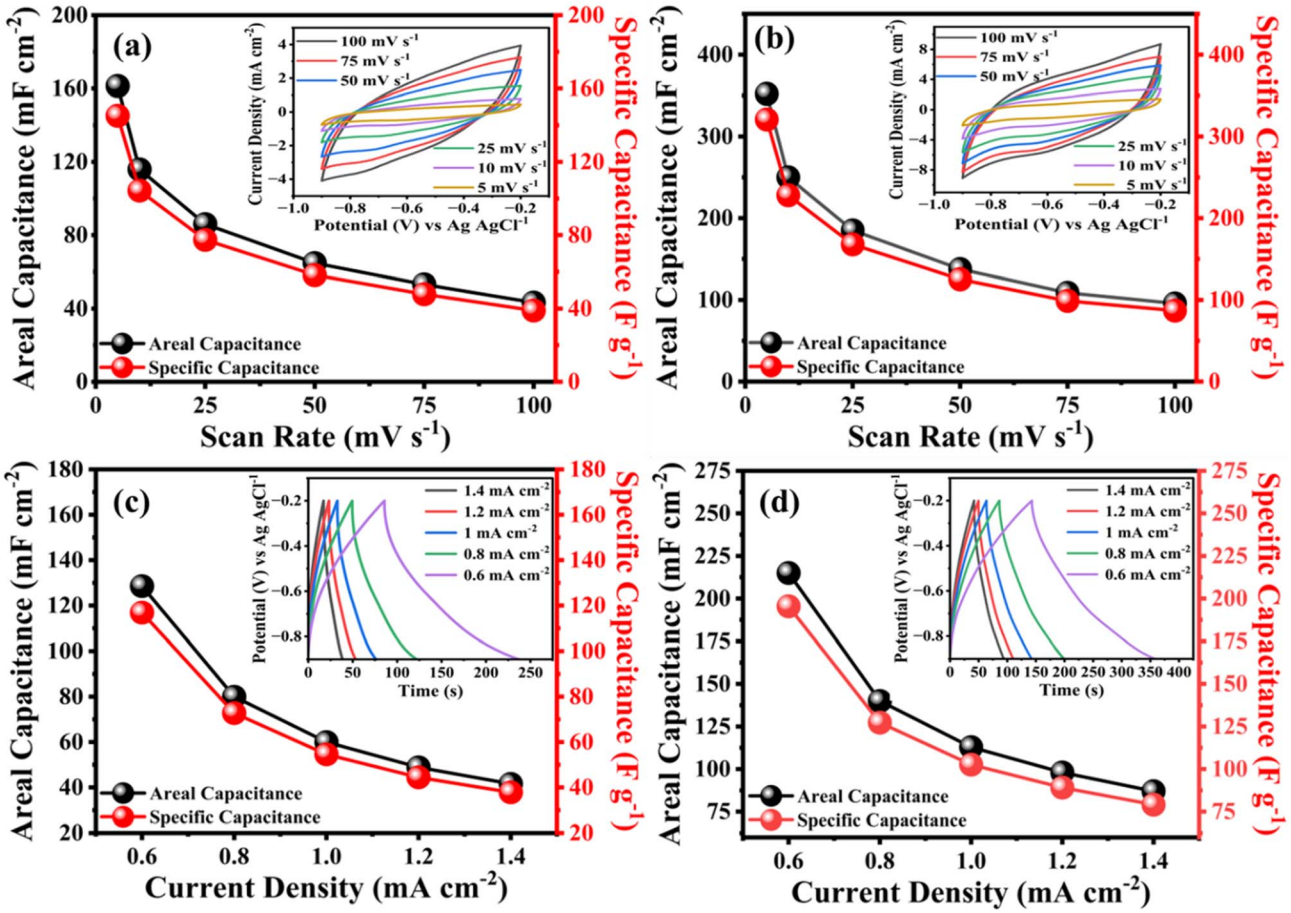

Fig. 11 Areal and specific capacitance of (a) complex **1** and (b) complex **2** as a function of scan rate ranging from 5 to 100 mV s^{-1}; insets: corresponding CV curves. Areal and specific capacitance of (c) complex **1** and (d) complex **2** at various current densities; insets: corresponding GCD curves.

controlled process, characteristic of pseudocapacitive materials. This behaviour likely originates from the redox-active chromium-triradical species within the complex, contributing to faradaic charge storage.[8]

The combined EDLC and pseudocapacitive contributions thus impart complex **2** with enhanced charge storage capability and electrochemical reversibility across varying scan rates. Complex **2** (E = Se) outperforms complex **1** (E = S) in terms of areal capacitance, specific capacitance, and pseudocapacitive contribution, likely due to its enhanced redox activity and improved ionic accessibility. This can be rationalized because the C=Se bond in **2** is significantly more polar in nature than the C=S bond in **1**.[39b] Furthermore, galvanostatic charge–discharge (GCD) measurements were conducted for the complex **1** and **2** electrodes within the same potential window at various current densities to assess their capacitive behaviour further. Unlike CV, which applies a variable potential and records the resulting current response, GCD involves charging and discharging the electrode at a constant current between fixed voltage limits, offering valuable insights into charge storage capacity.[53,54] The GCD curves of both complex **1** (Fig. 11(c) inset) and complex **2** (Fig. 11(d) inset) exhibited slight variation from symmetrical triangular shapes, indicative of pseudocapacitive behavior as expected for a redox active material.

GCD measurements revealed that the electrodes of complex **1** (Fig. 11(c)) and complex **2** (Fig. 11(d)) exhibited specific capacitances of 37.8 and 77.2 F g^{-1} (areal capacitances: 41.6 and 85.0 mF cm^{-2}, respectively) at a current density of 1.4 mA cm^{-2}. Remarkably, these values increased to 115.6 and 194.6 F g^{-1} (areal capacitances: 127.2 and 214.1 mF cm^{-2}, respectively) at a lower current density of 0.6 mA cm^{-2}. This trend reflects the characteristic decline in specific capacitance with increasing current density, which is typically attributed to limited ion diffusion and reduced accessibility of electroactive sites at higher charge–discharge rates.[55,56] The significant enhancement in charge storage capacity at lower current densities suggests that the electrode of complex **2** offers superior electrochemical performance.

Additionally, electrochemical impedance spectroscopy (EIS) was employed to investigate the electrical conductivity, charge-transfer behaviour, capacitive characteristics, and ion transport dynamics of these Cr(III)-triradical -based electrodes.[57,58] The Nyquist plots, presented in Fig. 12(a) and (b) for complex **1** and complex **2**, respectively, were recorded over a frequency range of 100 mHz to 10 kHz. The experimental data were modelled using

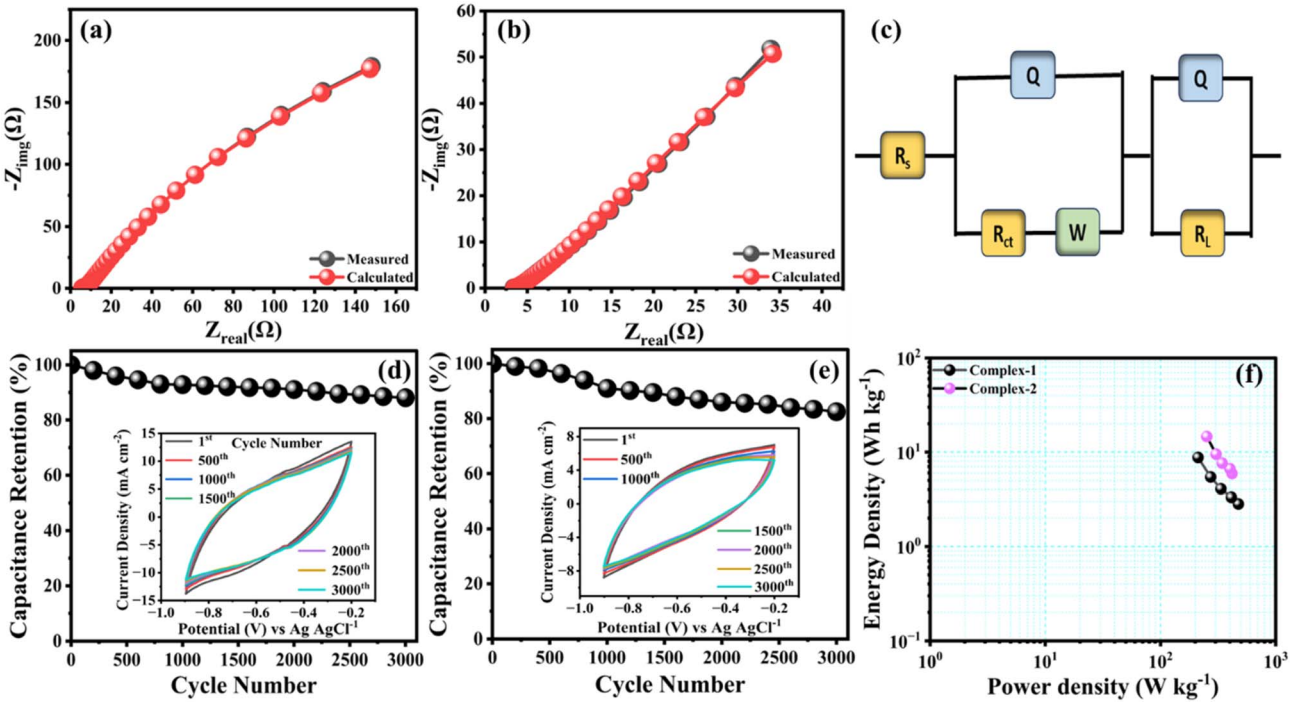

Fig. 12 Nyquist plot of (a) complex **1** and (b) complex **2**, (c) Nyquist plot circuit fitted for complex **1** and **2**, capacitive retention of (d) complex **1** and (e) complex **2** for 3000 CV cycles [(d) for **1** and (e) for **2**; 1st, 500, 1000, 1500, 2000, 2500, and 3000, inset bottom] at 200 mV s^{-1}, and (f) Ragone plot showing energy and power densities of complex **1** and **2** electrodes.

ZSimpWin software and fitted to the equivalent circuit R(Q(RW)(QR) as shown in Fig. 12(c). In this circuit, R_s represents the solution resistance, encompassing the contributions from the electrolyte, the stainless steel (SS) current collector, and the electrode–electrolyte interface. The R_{ct} element corresponds to the charge-transfer resistance, reflecting interfacial kinetics associated with redox reactions at the electrode surface. Meanwhile, R_L accounts for leakage current, providing insight into mass transport limitations during electrochemical operation.[59–61]

EIS demonstrates that the electrode based on complex **2** exhibits markedly improved electrochemical properties compared to complex **1**. Specifically, complex **2** shows a much lower solution resistance ($R_s = 0.1\ \Omega$) than complex **1** ($R_s = 2.2\ \Omega$), indicating enhanced electronic conductivity and reduced electrolyte/contact resistance. In addition, the charge-transfer resistance of complex **2** is slightly lower ($R_{ct} = 3.5\ \Omega$) than that of complex **1** (4.7 Ω), suggesting more favourable interfacial electron-transfer kinetics. After 3000 CV, complex **2** retained 87.3% as shown in Fig. 12(d) of its initial capacitance, outperforming complex **1**, which retained 81.2% as displayed in Fig. 12(e). The enhanced electrochemical stability of complex **2** can be attributed to its lower resistance values, which minimise energy losses and structural deterioration over prolonged cycling, underscoring its potential for durable high-performance energy storage applications.

Table 1 Summary of supercapacitor studies of Cr based compounds and complexes **1–2**

Material	Substrate	Electrolyte	Voltage window (V)	Specific capacitance (F g^{-1})	Capacitance retention (%) @ cycles	Ref.
CrO_3/SWCNT		6 M KOH	0–0.8	60@1 mV s^{-1}	100 @ 10 000	10
Cr/GO/POAP	Si/SiO_2	0.1 M $HClO_4$	0–1	354@0.5 A g^{-1}	94 @5000	9
Cr_2O_3/c	Graphite sheet	3 M KOH	−0.3–0.5	68@5 mV s^{-1}	86 @3000	14
Cr_2O_3/c//AC			0–1.5	21@5 mV s^{-1}	95 @3000	14
Cr_2O_3/MWCNT	Nickel grid	1 M KOH	−0.04–0.46	257@0.25 A g^{-1}	88 @3000	11
Cr_2O_3/rGO	Nickel foam	2 M KOH	0–0.7	310@1.75 A g^{-1}	92 @3500	13
LiCl/$CrCl_3$	PCGF	18 M LiCl and 0.5 M $CrCl_3$	0–1.5	1546 mAh g^{-1} (theoretical capacity)	95.4 @ 30 000	8
Complex **1**	Stainless steel	1 M LiCl	−0.2–0.9	145.2@5 mV s^{-1}	81.2 @3000	**This work**
Complex **2**	Stainless steel	1 M LiCl	−0.2–0.9	32 @5 mV s^{-1}	87.3 @3000	**This work**

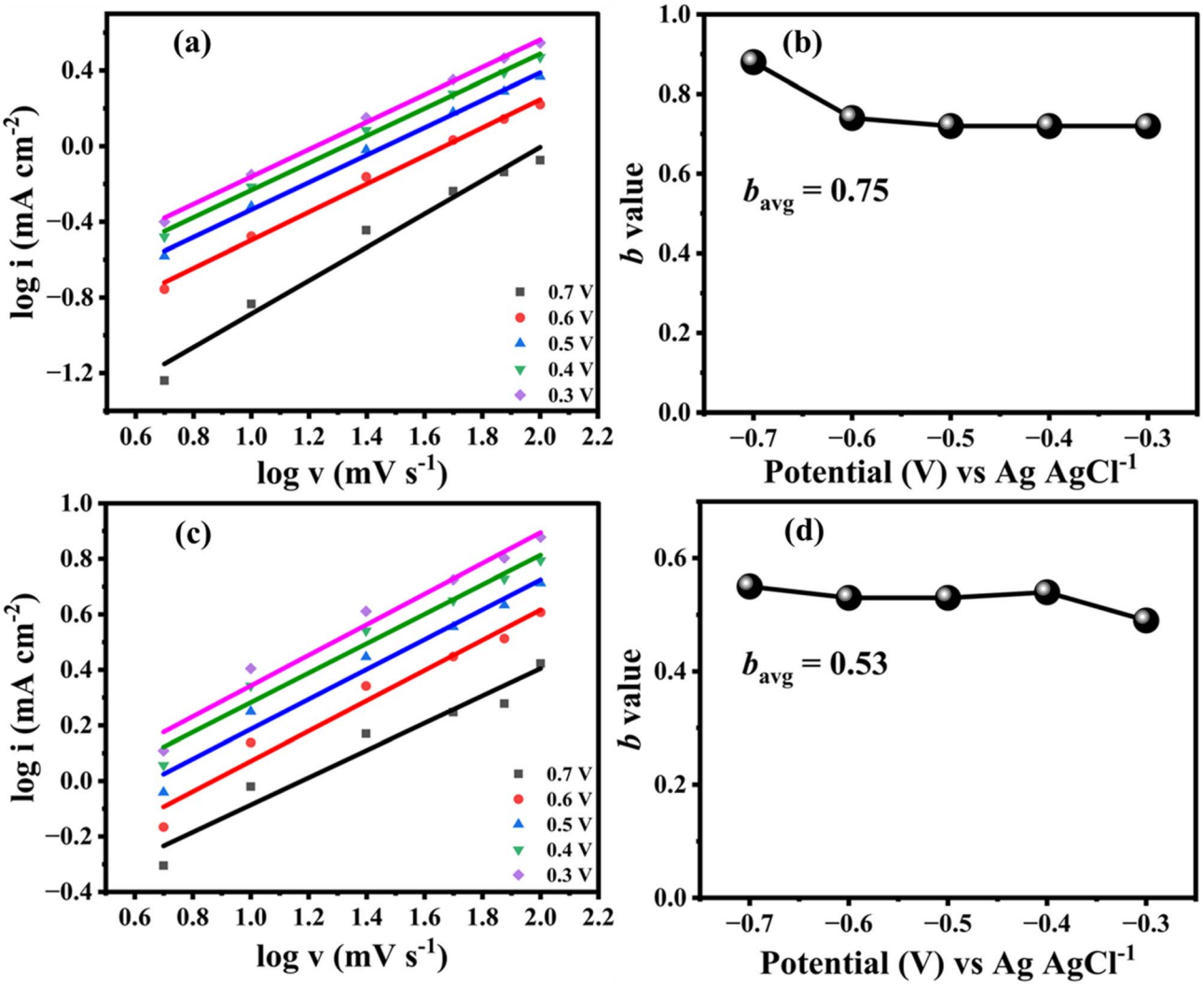

Fig. 13 Power law plots for (a) complex **1** and (c) complex **2**, along with the corresponding *b* values derived from their respective slopes, are shown in (b) for complex **1** and (d) for complex **2**.

The Ragone plot of complexes **1** and **2**, as presented in Fig. 12(f), is a critical tool for evaluating supercapacitor efficiency by highlighting the trade-off between energy density and power density.[62,63] Complex **1** exhibits a maximum energy density of 8.76 Wh kg^{-1} at a power density of 211 W kg^{-1}, and maintains a stable energy density of 2.83 Wh kg^{-1} even at its peak power density of 474 W kg^{-1}, indicating excellent rate performance. In contrast, complex **2** shows a higher energy storage capability, achieving a maximum energy density of 14.63 Wh kg^{-1} at 252 W kg^{-1}, and retains the same energy density of 2.83 Wh kg^{-1} at a power density of 417 W kg^{-1}. These results suggest that while complex **1** is better suited for high-power applications due to its superior rate capability, complex **2** is more effective in delivering higher energy output, making it advantageous for energy-demanding storage applications.

This work reports two discrete molecular chromium(III) complexes (**1** and **2**) directly deposited onto low-cost, commercially available stainless-steel substrates. Despite the comparatively lower intrinsic conductivity of stainless steel relative to conventional high-performance current collectors, complex **1** exhibits a specific capacitance of 145.2 F g^{-1} at 5 mV s^{-1} with 81.2% retention after 3000 cycles, while complex 2 delivers a substantially higher value of 320.2 F g^{-1} with 87.3% retention in 1 M LiCl within a potential window of −0.2 to −0.9 V. These electrochemical metrics are comparable to, and in some cases surpass, those reported for chromium-based electrodes in the literature, particularly when considering that the present complexes were evaluated in their pristine molecular form rather than within composite architectures. This performance underscores their inherent charge-storage capability. Furthermore, the use of stainless steel as the current collector provides a more realistic and application-oriented assessment than highly conductive substrates such as nickel foam, which can inflate apparent capacitance through parasitic effects. The combined advantages of chemical stability, mechanical robustness, corrosion resistance, and straightforward electrode fabrication render this system a scalable and cost-effective platform, with clear potential for further enhancement

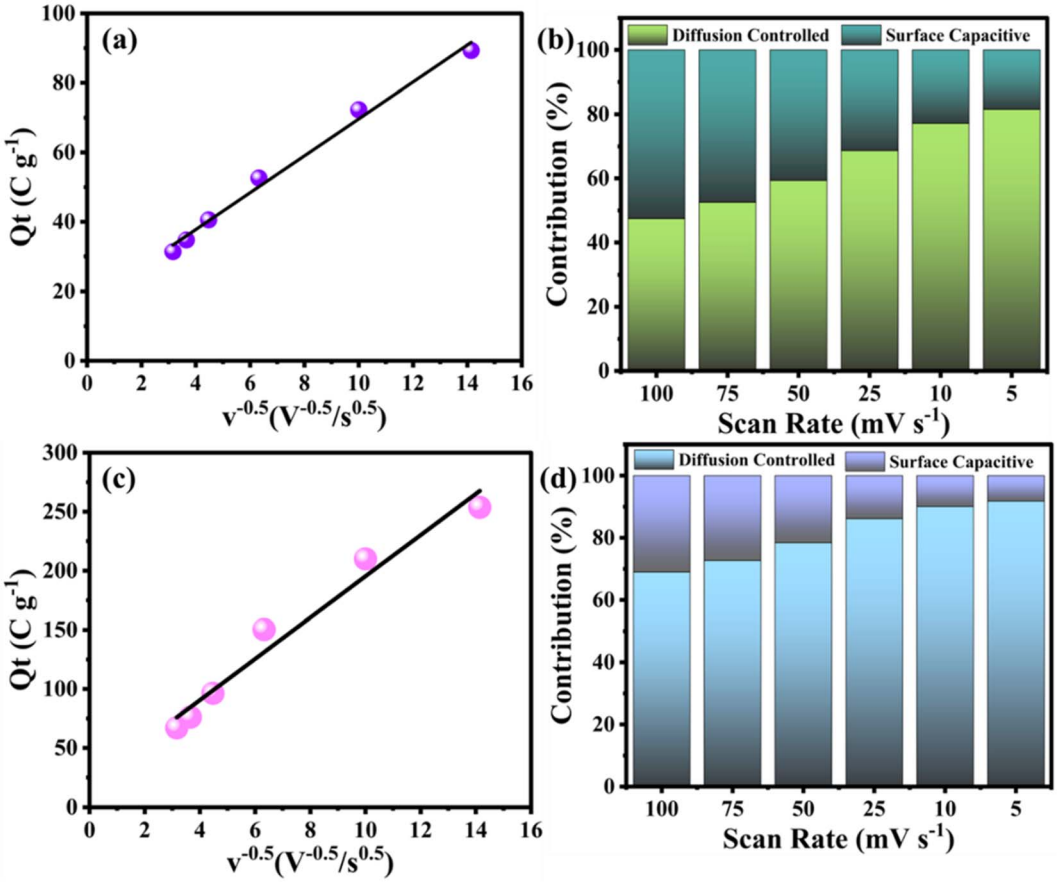

Fig. 14 Plots of total charge Q_t against the inverse square root of the scan rate of (a) complex **1** and (c) complex **2**, and corresponding plots showing the percentage contributions of each mechanism to the total charge of (b) complex **1** and (d) complex **2** at different scan rates.

through future composite integration or EDLC-hybridization strategies.

To clearly evaluate and compare the electrochemical behavior of both complexes, Table 1 provides a summary of the essential parameters derived from cyclic voltammetry (CV), galvanostatic charge–discharge (GCD) tests, and long-term stability assessments.

The kinetics of these charge storage processes [capacitive (non-faradaic) and redox (faradaic)] can be evaluated through a power-law relationship, which helps determine whether the behaviour is surface-controlled or diffusion-limited: $i = a\nu^b$,[64,65], where i represents the current density, ν is the scan rate, and a and b are fitting constants. The exponent b provides insight into the dominant charge storage mechanism. A b value close to

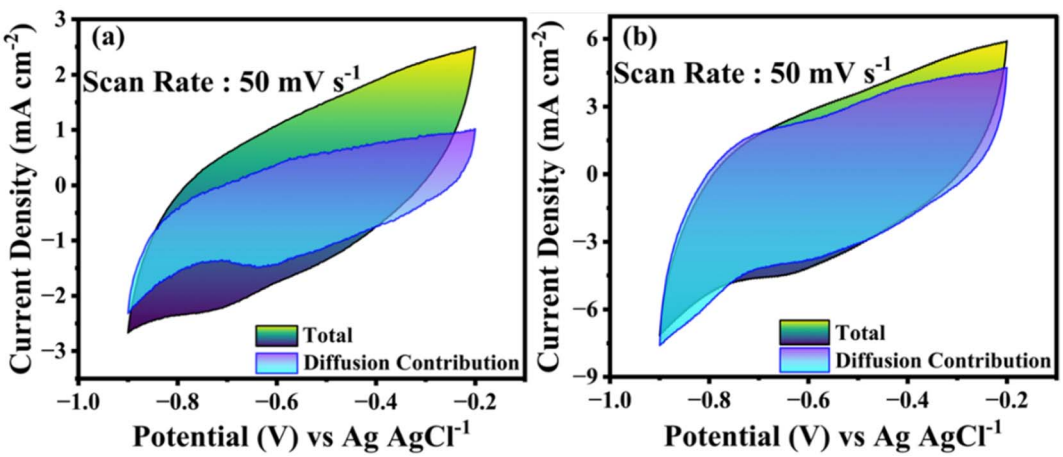

Fig. 15 CV plot of total and diffusion-controlled capacitance contributions for (a) complex **1** and (b) complex **2** at a 50 mV s^{-1} scan rate.

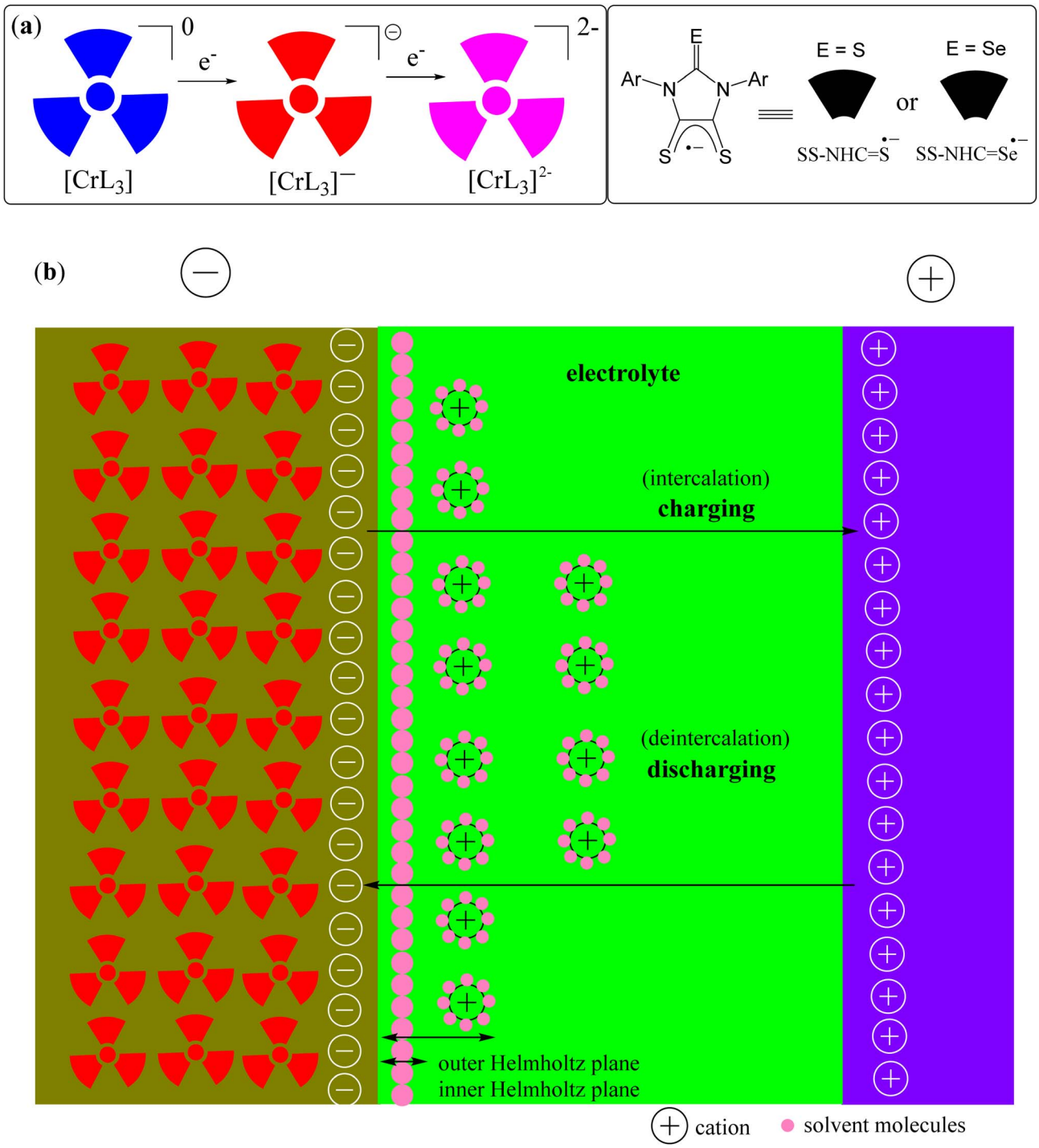

Fig. 16 (a) Successive one-electron reductions of the Cr(III)-triradical complex, [Cr(III)(SS-NHC = E)$_3$]. (b) Pseudo supercapacitor anode made of the Cr(III)-triradical complex, [Cr(III)(SS-NHC = E)$_3$]. Blue, red and pink propellers represent neutral, mono-anionic, and di-anionic forms of [Cr(III)(SS-NHC = E)$_3$]. Each blade-like black-coloured symbol represents the dithiolene ligand (SS-NHC = E), which could be either the radical mono-anionic and/or non-radical dianionic form here. From the electrochemical studies, it was found that complex **2** predominantly functions through a diffusion-controlled process (pseudo supercapacitor)[87], which has been elaborated in the figure.

1.0 indicates a surface-controlled capacitive process, while an a value near 0.5 reflects a diffusion-limited intercalation mechanism.[66,67] This evaluation is crucial for optimising electrode materials and tailoring them for either high-power or high-energy applications. To determine the b value, a plot of $\log(i)$ *versus* $\log(v)$ was constructed within the potential range of −0.3 to −0.7 V for both complexes **1** and **2**, as shown in Fig. 13(a) and (c). The slope of the linear fit provides the b value, which helps identify the charge storage mechanism. Fig. 13(b) and (d) show the potential-dependent variation of b, with

average values of 0.75 and 0.53 for **1** and **2**, respectively. These values suggest that complex **1** exhibits a mixed mechanism, dominated by diffusion-controlled pseudocapacitive behaviour with a notable surface capacitive contribution. In contrast, complex **2** mainly follows a diffusion-controlled mechanism with minimal surface capacitive involvement. This difference is further supported by the CV profiles, where complex **2** shows broader and more intense redox peaks, indicative of diffusion-governed charge storage, while complex **1** displays characteristics of both surface and redox-based processes. To gain a more detailed understanding of the charge storage mechanism, Trasatti's analysis was employed to qualitatively distinguish between the surface-capacitive contribution (Q_s) and the diffusion-controlled contribution ($Q_d \propto \nu^{-0.5}$). The overall charge storage behaviour is described by using the following relationship.[68,69]

$$Q_t = Q_S + Q_d \text{ and } Q_t = Q_S + k\nu^{-0.5}$$

To further evaluate the charge storage behaviour, a plot of total charge (Q_t) *versus* the inverse square root of the scan rate was used to extract the surface capacitive contribution (Q_s) from the *y*-intercept, as shown in Fig. 14(a) and (c). The relative contributions of surface-capacitive and diffusion-controlled mechanisms are illustrated in Fig. 14(b) and (d). While the surface-controlled charge remains relatively constant across different scan rates, the diffusion-controlled contribution becomes more prominent at lower scan rates. At a high scan rate of 100 mV s^{-1}, complex **1** displays a diffusion-controlled contribution of about 47.4%, which increases significantly to 81.5% at 5 mV s^{-1}. In comparison, complex **2** exhibits a stronger diffusion-dominated behaviour, contributing 68.9% at 100 mV s^{-1} and increasing to 91.8% at 5 mV s^{-1}. This comparison indicates that complex **2** favours diffusion-limited processes more than complex **1**, suggesting its higher reliance on ion transport within the bulk for charge storage.

Furthermore, the contribution of the diffusion-controlled process was also validated using Dunn's method. As shown in Fig. 15(a) and (b), the fitted results for **1** and **2** at a scan rate of 50 mV s^{-1} clearly distinguished the capacitive (green region) and diffusion-controlled (blue region) contributions to the total current response. Notably, complex **2** exhibits a significantly higher diffusion-controlled contribution of 88.54%, compared to 66.78% for complex **1**. This enhanced diffusion contribution in complex **2** is consistent with earlier electrochemical analyses and indicates improved ion transport and redox activity, further confirming its superior pseudocapacitive behaviour over complex **1**. To rationalise the supercapacitor behaviour, CV measurements (Fig. 7) and Hirshfeld surface maps (Fig. S36 and S38) of complexes **1–2** were referred.

In the past, several studies have investigated chromium-based nanocomposites, such as chromium oxides and sulfides, for supercapacitor applications, motivated by chromium's variable oxidation states and rich redox chemistry. Most prior reports primarily rely on inorganic chromium oxides incorporated into composite architectures, often with conductive supports, to enhance electrochemical performance. Lota *et al.*[10] demonstrated that decorating single-walled carbon nanotubes with CrO_3 primarily improves cycling stability, achieving nearly 100% capacitance retention over 10 000 cycles, albeit with modest capacitance values. Ashtiani *et al.*[9] highlighted the role of chromium–graphene interfacial interactions in a Cr–GO hybrid system, where surface functionalisation enabled high pseudocapacitive contribution and resulted in

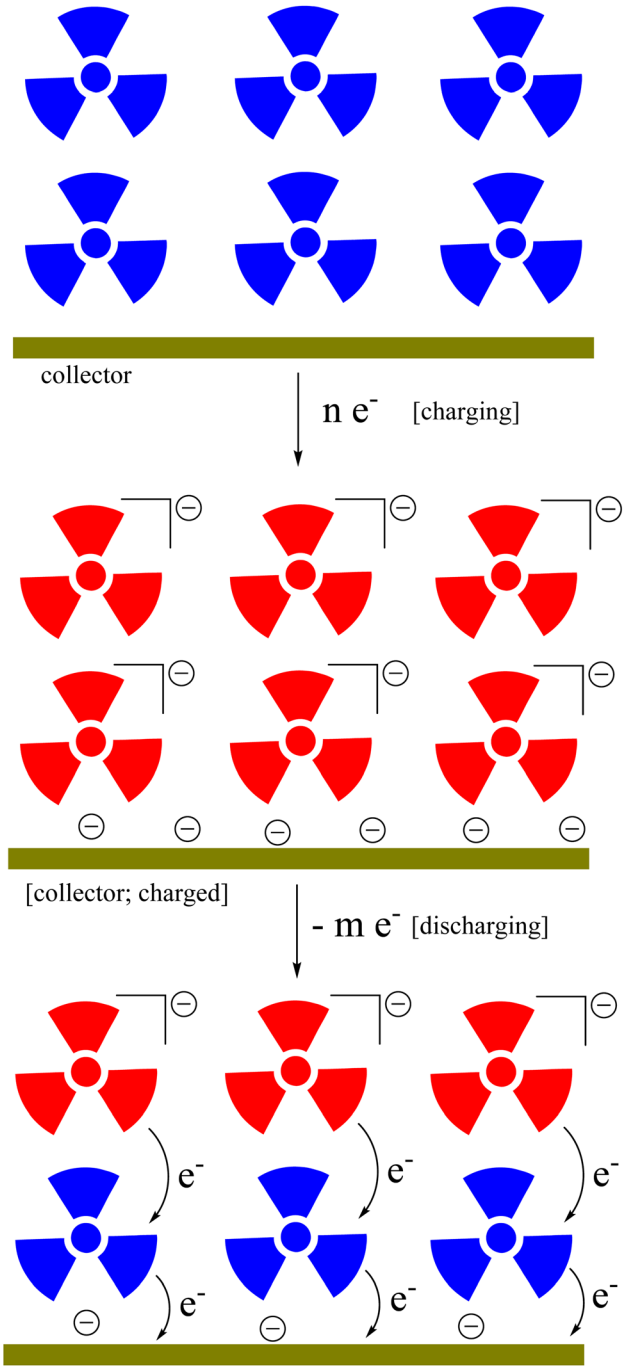

Fig. 17 Plausible mechanism for charging and discharging of an anode made of the Cr(III)-triradical complex *via* the pseudo supercapacitive pathway. The blue and red propellers represent the neutral and mono-anionic Cr(III)-triradical complex.

a specific capacitance of 354 F g^{-1}. Kansal *et al.*[14] showed that morphology-controlled Cr_2O_3 nanostructures facilitate reversible Cr^{3+}/Cr^{4+} redox reactions, leading to improved capacitance retention, while also enabling asymmetric device operation in an extended voltage window of 1.5 V. Shafi *et al.*[11,12] further demonstrated that highly conductive current collectors, such as nickel grids or nickel foam, significantly enhance the apparent capacitance of Cr_2O_3-based electrodes through improved charge transport. Similarly, Chen *et al.*[13] confirmed that coupling Cr_2O_3 with carbon nanotubes markedly reduces capacitance fading, underscoring the importance of carbonaceous additives in stabilising chromium oxide electrodes. More recently, Sun *et al.*[8] introduced a Cr-ion storage system employing a highly concentrated electrolyte, achieving exceptional long-term stability and low-temperature performance, emphasising electrolyte engineering rather than intrinsic material properties as the dominant performance factor. The oxidation state of the central chromium ion in complexes **1–2** remains unchanged functioning through redox-active radical ligands bonded to the Cr(III) ion [Fig. 16a].

3.1 Organic molecules and radicals for electrochemical energy storage

Over the past several years, redox-active stable organic radicals [discrete molecules and polymers containing radicals], were

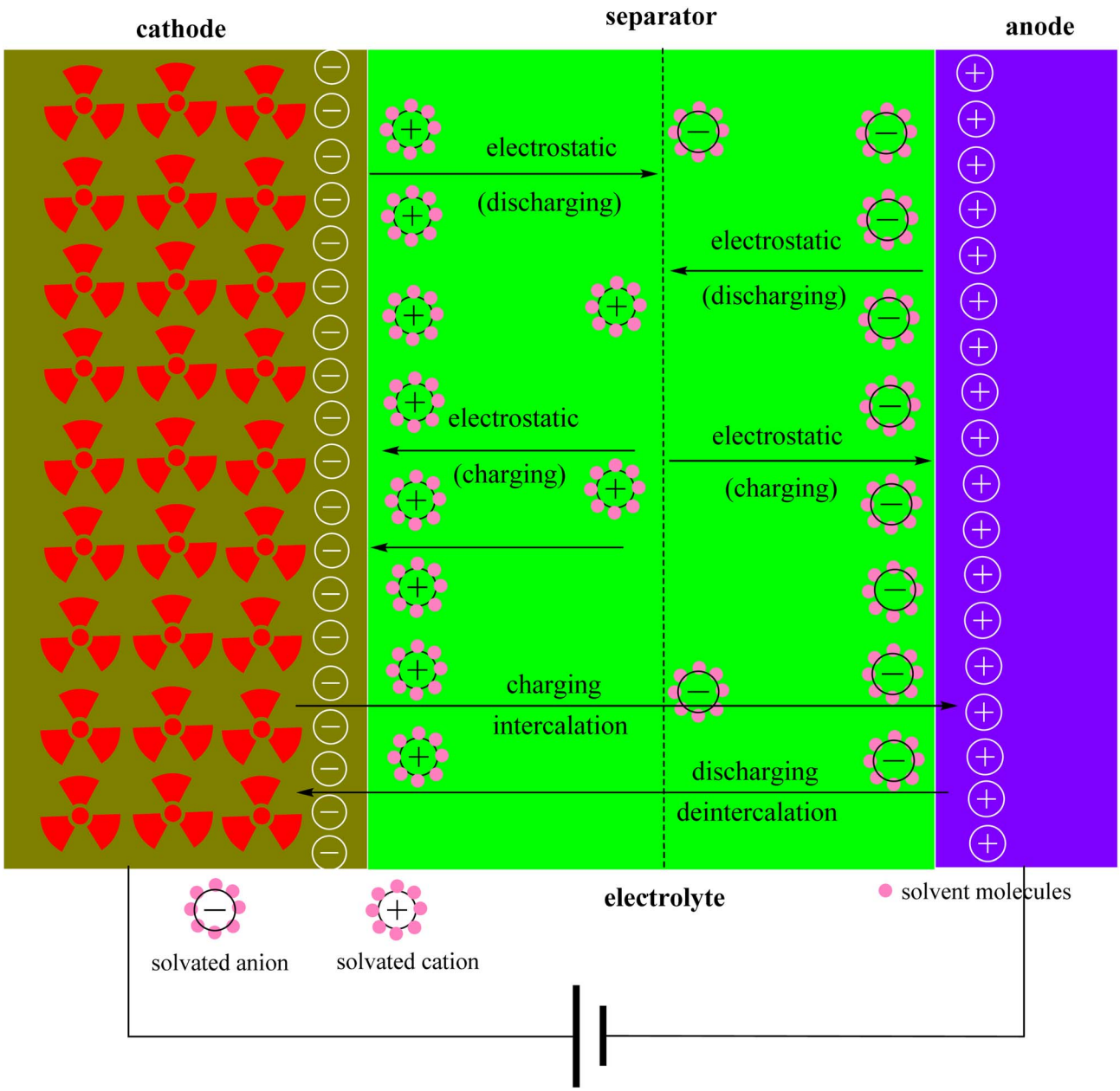

Fig. 18 Proposed mechanism for charging and discharging of an anode made of the Cr(III)-triradical complex *via* the hybrid supercapacitive pathway.

employed for electrochemical energy storage, taking advantage of the ability to reversibly transfer single electron or multiple electrons transfer without the decomposition or irreversible unavoiding and underised side reactions with another species in the neutral or charge state.[70–77] In addition, stable radicals were shown to act as redox shuttles in Li-ion batteries for overcharge protection.[78] The importance and reports on stable radicals for electrochemical energy storage have been summarised by Wheeler *et al.*[77] Three decades ago, organosulfur compounds [lithium carbamate; $(R_2N)_2$-CS_2Li] were studied towards electrochemical energy storage application in a battery, showing the highest capacities, but were limited due to poor cyclability and sluggish redox kinetics.[79,80] In comparison, redox-active closed shell organic compounds, which can form reversible open-shell radical anions and closed-shell dianions during electrochemical battery performance, possess higher power capabilities, high redox potentials, and good tunability, but suffer from the lowest capacities.[81–84] Seferos *et al.* summarised the utility and the upsurge of organic molecule-based electrode materials for energy storage.[85] In the past, S and Se containing stable organic radicals were also shown to be significantly conducting and could be advantageous from the perspective of supercapacitor properties.[41] This property generally enhances the supercapacitive performances.

In this context, the dithiolene ligands [L = SS-NHC = E; E = S, Se] have the ability to adopt different electronic states, a singlet dianion (L^{2-}), doublet mono-anionic radical ($L^{\bullet-}$), and neutral singlet (L) depending on the electrochemical potential [$L^{2-} \rightarrow L^{\bullet-} \rightarrow L^{0}$] (Fig. 1b).[22–25,39b] The C=Se bond of ligand SS-NHC = Se is inherently more polar than the C=S bond of ligand SS-NHC = S due to the poor orbital overlap between the 2p orbital of the C-atom and 4p orbital of the Se-atom (Fig. 1c). Both complex **1** and complex **2** are redox active in the voltage range from 0.0 to 1.0 V in THF solution (Fig. 7) with $E_{1/2}$ = −0.51 V (complex **1**) and $E_{1/2}$ = −0.72 V (complex **2**), respectively. Electrically neutral Cr(III)-triradical complexes [CrL_3; complex **1**, complex **2**] are theoretically found to be electron hungry [$CrL_3 + e^- \rightarrow CrL_3^-$; Fig. 16(a)]. The electron affinity values of **1′–2′** [Dipp groups in complexes **1–2** replaced by Me group in **1′–2′** for simplicity of calculation] were computed to be favourable by 101.5 and 105.4 kcal mol^{-1}, respectively, at the B3LYP-D3(BJ)/def2-TZVPP level of theory. The best supercapacitor performance was shown in the voltage range from −0.2 to −0.9 V (Fig. 15).

3.2 Mechanism of pseudo-capacitive behaviour of Cr(III)-triradical complexes

There are three types of supercapacitors: electric double layer capacitors (EDLCs), pseudo-capacitors and hybrid supercapacitors.[86] Both the Cr(III)-triradical complexes (**1–2**) are moderately stable in air in the solid state at room temperature (Fig. S2 and S3). Cycling stabilities of complexes **1–2** are 81.2% and 87.3% after 3000 cycles, respectively (Fig. 12d and e). Electrochemical analyses showed that complex **1** operates *via* a mixed surface-capacitive and diffusion-controlled mechanism, while complex **2** predominantly functions through a diffusion-controlled process, enabling better charge transport and superior pseudocapacitive performance compared to complex **1**.

The electrode made of complex **2** (Cr–Se) stores electrons on one of the ligands [L = SS-NHC = Se] of the CrL_3 forming anionic complex CrL_3^- [$CrL_3 + e- \rightarrow CrL_3^-$; Fig. 16(a)] during charging of the electrode Fig. 17]. The electrons are gradually lost from the surface of the electrode and adjacent anionic complex CrL_3^- [anionic form of complex **1**] leading to the formation of neutral complex CrL_3 [complex **1**] in the working potential range [-0.2 to −0.9 V]. The electron from anionic complex **1** [CrL_3^-] can be transferred from the inner layer containing anionic complex CrL_3^- to the neutral complex CrL_3 and finally to the electrode, as shown in Fig. 17. The electrochemical behaviors suggest that complex **1** is more like a hybrid supercapacitor meaning a combination of EDLC and pseudocapacitive behavior [*i.e.* mixed surface- and diffusion-controlled mechanism; exhibiting both faradaic and non-faradaic processes] (Fig. 18).[88] In comparison, complex **2** predominantly functions through a diffusion-controlled process (pseudo supercapacitor)[87] which is elaborated in Fig. 16.

4 Conclusion

In conclusion, we have successfully isolated two redox active elusive Cr(III)-triradical complexes (**1–2**) as dark crystalline solids containing three anionic dithiolene radical ligands for the first time, achieving air stability for a day, unlike the anionic Cr(III)-diradical complexes synthesized by Wieghardt *et al.*, which could not be extended to isolable triradicals.[27,28] They have been structurally characterized by X-ray single-crystal diffraction. The spin ground state and nature Cr(III)-radical interaction have been studied by magnetic measurements. These complexes have been further spectroscopically characterized by UV-vis, IR, Raman, and EPR measurements. The redox properties have been studied by CV measurements, showing the formation of anionic doublet species $(\mathbf{1/2})^{\bullet-}$ which have been characterized by EPR and UV-vis measurements in solution as well. The nature of chemical bonding and pair-wise bonding interactions between the central Cr(III) ion and anionic radical ligand have been studied by EDA-NOCV analysis. The distributions of electron densities in both neutral complexes **1/2** and their corresponding anions $(\mathbf{1/2})^{\bullet-}$ were studied by computation of Mulliken spin densities. Finally, these redox-active, well-characterised, atomically precise Cr(III)-triradical complexes **1–2** were coated on stainless-steel substrates. Interestingly, they exhibited good to excellent supercapacitor performance. The detailed supercapacitive studies showed that complex **2** consistently outperforms complex **1**. At 5 mV s^{-1}, specific capacitances were 145.21 F g^{-1} for complex **1** and a markedly higher 340.9 F g^{-1} for complex **2**, both centred at around $E_{1/2}$ = −0.72 V. Cycling stability after 3000 cycles was also superior for complex **2** (87.3%) compared to complex **1** (81.2%). The enhanced performance of complex **2** is attributed to substituting E = S of the SS-NHC = $E^{\bullet-}$ ligand in complex **1** with the heavier chalcogenide E = Se in complex **2**, which improves redox activity, electrical conductivity, and ion

transport. Ragone plot analysis further confirmed the advantage of complex **2**, delivering 14.63 Wh kg^{-1} at 252 W kg^{-1}, compared to 8.76 Wh kg^{-1} at 211 W kg^{-1} for complex **1**. Electrochemical analyses were carried out by power-law, Trasatti, and Dunn's methods, which revealed that complex **1** operates *via* a mixed surface- and diffusion-controlled mechanism, whereas complex **2** predominantly follows a diffusion-controlled process, enabling more efficient charge transport and superior pseudocapacitive performance. To the best of our knowledge, this represents the first supercapacitive study of a stable metal-radical complex, forging a direct link between metal radical redox chemistry and electrochemical energy storage while establishing a new design paradigm for molecular supercapacitors powered by carbene-based radical ligands.[25,26,39b,70–88]

Author contributions

Sujit Das: synthesis, methodology, formal analysis, investigation, DFT, CV, data curation, writing – original draft. Mayur Thosare: supercapacitive studies, formal analysis, investigation, data curation, writing – original draft. Saurav Ghosh: methodology, formal analysis. Subuhan Ahamed: EPR and Raman analysis and writing. Harsha S. Karnamkkott: DFT studies and writing. T Kedara Shivasharma: supercapacitive studies, formal analysis, investigation, data curation, writing – original draft. Björn Schwarz: magnetic measurements. Babasaheb R. Sankapal: conceptualisation, writing – review & editing, supervision, funding acquisition. Liviu Ungur: theoretical calculations. Kartik Chandra Mondal: conceptualisation, writing – review & editing, supervision, funding acquisition.

Conflicts of interest

There are no conflicts to declare.

Data availability

CCDC 2408554, 2412264 and 2495748 contain the supplementary crystallographic data for this paper.[89a–c]

The data supporting this article have been included as part of the supplementary information (SI). Supplementary information: synthesis, characterisation, CV, EPR, NMR plots, figures, tables, EDA-NOCV methods, and optimised geometry/coordinates. See DOI: https://doi.org/10.1039/d5ta08423g.

Acknowledgements

S. D. thanks CSIR for the fellowship. K. C. M. thanks SERB, New Delhi (ECR/2016/000890). T. K. S. is thankful to DST (DST/INSPIRE/03/2022/000141) for providing an INSPIRE fellowship. B. R. S. gratefully acknowledges ANRF (CRG/2023/001184) and DST-FIST (SR/FST/PSI/2017/5 (C)) projects, K. C. M. IIT Madras for research facilities, HPCE Aqua Cluster of IIT Madras for theoretical calculation facilities, and IITM/IISER Tirupati for single-crystal XRD facilities. KCM thanks DST-FIST for computational and other facilities at IIT M.

References

1 A. Dutta, S. Mitra, M. Basak and T. Banerjee, *Energy Storage*, 2023, **5**, e339.
2 R. K. Azega, A. D. Smith, N. R. Chowdhury, A. Vyas, Q. Li, M. Haque, Q. Xun, X. Zhang, S. Thurakkal, T. Thiringer, P. Enoksson and P. Lundgren, *Sustainable Mater. Technol.*, 2024, **41**, e01111.
3 C. Lu and X. Chen, *Acc. Chem. Res.*, 2020, **53**, 1468–1477.
4 (*a*) C. B. Evans, *Electrochemical Supercapacitors: Scientific Fundamentals and Technological Applications*, Berlin, Germany, Springer, 1999, pp. 1–8; (*b*) C. B. Evans, *J. Electrochem. Soc.*, 1991, **138**, 1539–1548.
5 C. B. Evans, Electrochemical Capacitors — Their Nature, Function and Applications, *Electrochemistry Encyclopedia*, 2012.
6 H. Zhai, J. He, S. Shi, M. Liu, Z. Wang and Z. Jin, *J. Mater. Chem. A*, 2025, **13**, 25626–25643.
7 N. Katsuhiko, N. Wako, A. Shintaro, M. Jun-Ichi and K. Takeo, *Acc. Chem. Res.*, 2013, **46**, 1075–1083.
8 B. Sun, N. Wang, X. Xie, L. Zhong, L. He, M. Xiang, K. Liang and W. Hu, *Angew. Chem., Int. Ed.*, 2024, **63**, e202408569.
9 A. A. Ashtiani, E. Kowsari, V. Haddadi-Asl, M. Yousefi, H. R. Naderi, A. Chinnappan and S. Ramakrishna, *J. Mol. Liq.*, 2020, **315**, 113697.
10 G. Lota, E. Frackowiak, J. Mittal and M. Monthioux, *Chem. Phys. Lett.*, 2007, **434**, 73.
11 I. Shafi, E. Liang and B. Li, *J. Alloys Compd.*, 2021, **851**, 156046.
12 I. Shafi, Y. Liu, G. Zeng, Z. Li, B. Li and E. Liang, *SN Appl. Sci.*, 2020, **2**, 1836.
13 B. Chen, Y. Wang, C. Li, L. Fu, X. Liu, Y. Zhu, L. Zhang and Y. Wu, *RSC Adv.*, 2017, **7**, 25019.
14 S. Kansal, J. Halder, D. Mandal, R. Rahul, S. Priya, P. De, V. Sharma, A. K. Srivastava, T. Singh and A. Chandra, *Mater. Sci. Eng., B*, 2023, **293**, 116438.
15 A. A. Leitch, X. Yu, S. M. Winter, R. A. Secco, P. A. Dube and R. T. Oakley, *J. Am. Chem. Soc.*, 2009, **131**, 7112.
16 B. Chen, Z. Lu, S. Feng, Z. Zhou and C. Lu, *ACS Energy Lett.*, 2023, **8**, 1096.
17 M. D. Najafi, E. Kowsari, H. R. Naderi, A. Chinnappan, S. Ramakrishna, A. Ehsani and A. Shokravi, *Compos. Sci. Technol.*, 2021, **211**, 108844.
18 G. Liu, G. Wang and Z. Jin, *Energy Fuels*, 2024, **38**, 12251.
19 K. Adib, B. Chameh and F. Gravand, *J. Energy Storage*, 2020, **12**, 931.
20 R. N. Bulakhe, A. P. Nguyen, C. Ryu, J. M. Kim and J. B. In, *Materials*, 2023, **16**, 6598.
21 L. Vivas, A. Jara, J. M. Garcia-Garfido, D. Serafini and D. P. Singh, *ACS Omega*, 2022, **7**, 42446.
22 (*a*) A. L. Balch, I. G. Dance and R. H. Holm, *J. Am. Chem. Soc.*, 1968, **90**, 1139; (*b*) I. G. Dance and T. R. Miller, *Inorg. Chem.*, 1974, **13**, 525; (*c*) G. N. Schrauzer, V. P. Mayweg, H. W. Finck and W. Heinrich, *J. Am. Chem. Soc.*, 1966, **88**, 4604; (*d*) D. Sellmann, M. Geek, F. Knoch, G. Ritter and J. Dengler, *J. Am. Chem. Soc.*, 1991, **113**, 3819; (*e*) K. Ray, A. Begum,

T. Weyhermüller, S. Piligkos, J. van Slageren, F. Neese and K. Wieghardt, *J. Am. Chem. Soc.*, 2005, **127**, 4403–4415; (*f*) K. Ray, E. Bill, T. Weyhermüller and K. Wieghardt, *J. Am. Chem. Soc.*, 2005, **127**, 5641–5654; (*g*) K. Ray, T. Weyhermüller, F. Neese and K. Wieghardt, *Inorg. Chem.*, 2005, **44**, 5345–5360; (*h*) A. K. Patra, E. Bill, E. Bothe, K. Chlopek, F. Neese, T. Weyhermüller, K. Stobie, M. D. Ward, J. A. McCleverty and K. Wieghardt, *Inorg. Chem.*, 2006, **45**, 7877–7890; (*i*) A. K. Patra, E. Bill, T. Weyhermüller, K. Stobie, Z. Bell, M. D. Ward, J. A. McCleverty and K. Wieghardt, *Inorg. Chem.*, 2006, **45**, 6541–6548.

23 Dithiolene Chemistry: Synthesis, Properties, and Applications, *Copyright © 2004 John Wiley & Sons, Inc. Book Series: Progress in Inorganic Chemistry*, ed. E. I. Stiefel, 2003, DOI: 10.1002/0471471933.

24 (*a*) R. Yu, K. Arumugam, A. Manepalli, Y. Tran, R. Schmehl, H. Jacobsen and J. P. Donahue, *Inorg. Chem.*, 2007, **46**, 5131–5133; (*b*) S. R. Boone, G. H. Purser, H. R. Chang, M. D. Lowery, D. N. Hendrickson and C. G. Pierpont, *J. Am. Chem. Soc.*, 1989, **111**, 2292–2299; (*c*) S. A. Attia, B. J. Conklin, C. W. Lange and C. G. Pierpont, *Inorg. Chem.*, 1996, **35**, 1033–1038; (*d*) C. Milsmann, S. Sproules, E. Bill, T. Weyhermüller, S. D. George and K. Wieghardt, *Chem.–Eur. J.*, 2010, **16**, 3628–3645; (*e*) A. Matamoros-Veloza, O. Cespedes, B. R. Johnson, T. M. Stawski, U. Terranova, N. H. de Leeuw and L. G. Benning, *Nat. Commun.*, 2018, **9**, 3125.

25 (*a*) Y. Wang, H. P. Hickox, Y. Xie, P. Wei, S. A. Blair, M. K. Johnson III, H. F. Schaefer and G. H. Robinson, *J. Am. Chem. Soc.*, 2017, **139**, 6859; (*b*) Y. Wang, P. M. Tran, B. Dzikovski, Y. Xie, P. Wei, Rains, H. Asadi, R. P. Ramasamy III, H. F. Schaefer and G. H. Robinson, *Organometallics*, 2022, **41**, 527; (*c*) Y. Wang, Y. Xie, P. Wei III, H. F. Schaefer and G. H. Robinson, *Dalton Trans.*, 2019, **48**, 3543.

26 (*a*) Y. Wang, Y. Xie, P. Wei, S. A. Blair, D. Cui, M. K. Johnson III, H. F. Schaefer and G. H. Robinson, *Angew. Chem., Int. Ed.*, 2018, **57**, 7865; (*b*) P. M. Tran, Y. Wang, B. Dzikovski, M. E. Lahm, Y. Xie, P. Wei, V. V. Klepov, H. F. Schaefer III and G. H. Robinson, *J. Am. Chem. Soc.*, 2024, **146**, 16340–16347.

27 R. R. Kapre, E. Bothe, T. Weyhermüller, S. D. George, N. Muresan and K. Wieghardt, *Inorg. Chem.*, 2007, **46**, 7827.

28 P. Banerjee, S. Sproules, T. Weyhermüller, S. D. George and K. Wieghardt, *Inorg. Chem.*, 2009, **48**, 5829.

29 A. Sokolowski, E. Bothe, E. Bill, T. Weyhermüller and K. Wieghardt, *Chem. Commun.*, 1996, 1671.

30 M. Wang, J. England, T. Weyhermüller, S.-L. Kokatam, C. J. Pollock, S. DeBeer, J. Shen, G. P. A. Yap, K. H. Theopold and K. Wieghardt, *Inorg. Chem.*, 2013, **52**, 4472.

31 E. Smith and G. Dent, *Modern Raman Spectroscopy – A Practical Approach*, John Wiley & Sons, Chichester, 2004., DOI: 10.1002/0470011831.

32 A. Matamoros-Veloza, O. Cespedes, B. R. Johnson, T. M. Stawski, U. Terranova, N. H. de Leeuw and L. G. Benning, *Nat. Commun.*, 2018, **9**, 3125.

33 (*a*) A. A. Jarzęcki, *J. Phys. Chem. A*, 2012, **116**, 571–581; (*b*) E. A. Soares, C. Téllez, S. A. Fortes, A. Coelho, O. Versiane, G. B. Ferreira, M. A. Mondragón and C. A. TéllezS, *J. Mol. Struct.*, 2022, **1256**, 132555.

34 Z. Cheng, H. Abernathy and M. Liu, *J. Phys. Chem. C*, 2007, **111**, 17997–18000.

35 C. Avril, V. Malavergne, R. Caracas, B. Zanda, B. Reynard, E. Charon, E. Bobocioiu, F. Brunet, S. Borensztajn, S. Pont and M. Tarrida, *Meteorit. Planet. Sci.*, 2013, **48**, 1415–1426.

36 S. I. Gorelsky, L. Basumallick, J. Vura-Weis, R. Sarangi, K. O. Hodgson, B. Hedman, K. Fujisawa and E. I. Solomon, *Inorg. Chem.*, 2005, **44**, 4947–4960.

37 G. Socrates, *Infrared and Raman Characteristic Group Frequencies: Tables and Charts*, John Wiley & Sons, 2004.

38 (*a*) S. Todorovic and M. Teixeira, *JBIC J. Biol. Inorg. Chem.*, 2018, **23**, 647–661; (*b*) H. G. M. Edwards, *Handb. Vib. Spectrosc.*, 2006, **3**, 1838–1871.

39 (*a*) C. B. Larsen, K. Ledbetter, D. R. Nascimento, E. Biasin, M. Qureshi, S. H. Nowak, D. Sokaras, N. Govind and A. A. Cordones, *Am. Chem. Soc.*, 2024, **146**, 28561–28571; (*b*) S. Das, A. Jain, S. Ahamed, B. Sahu, S. Suthar, B. Schwarz, C. L. Mascarenhas, S. Mondal, S. Banerjee, S. K. Kushvaha, H. W. Roesky and K. C. Mondal, *Angew. Chem., Int. Ed.*, 2025, e202507231, DOI: 10.1002/anie.202507231.

40 (*a*) S. Stoll and A. Schweiger, *J. Magn. Reson.*, 2006, **178**, 42–55; (*b*) S. Ye, *Magn. Reson. Lett.*, 2023, **3**, 43–60.

41 A. A. Leitch, X. Yu, S. M. Winter, R. A. Secco, P. A. Dube and R. T. Oakley, *J. Am. Chem. Soc.*, 2009, **131**, 7112.

42 C. Lu and X. Chen, *J. Mater. Chem. A*, 2019, **7**, 20158–20161.

43 M. Thosare, T. B. Deshmukh, R. N. Bulakhe, J. M. Kim and B. R. Sankapal, *J. Energy Storage*, 2025, **130**, 117338.

44 Y. Jiang and J. Liu, *Energy Environ. Mater.*, 2019, **2**, 30–37.

45 Y. Ren, Y. Liu, S. Wang, Q. Wang, S. Li, W. Wang and X. Dong, *Carbon Energy*, 2022, **4**, 527–538.

46 S. J. Panchu, K. Raju and H. C. Swart, *ChemElectroChem*, 2024, **11**, e202300810.

47 G. Tatrari, S. Bhowmick, A. Filippov, R. An and F. U. Shah, *Energy Storage*, 2024, **6**, e535.

48 D. N. Bangera, Y. N. Sudhakar and R. A. Nazareth, *RSC Adv.*, 2024, **14**, 28854–28880.

49 M. H. Gharahcheshmeh and K. U. A. Chowdhury, *Energy Adv.*, 2024, **3**, 2668–2703.

50 P. De, J. Halder, C. C. Gowda, S. Kansal, S. Priya, S. Anshu, A. Chowdhury, D. Mandal, S. Biswas, B. K. Dubey and A. Chandra, *Electrochem Sci Adv.*, 2023, **3**, e2100159.

51 M. M. Muzakir, Z. Zainal, H. N. Lim, A. H. Abdullah and N. N. Bahrudin, *RSC Adv.*, 2021, **11**, 26700–26709.

52 M. Shahzad, F. Ahmad, M. Ibraheem, A. Shakoor, S. M. Ramay, M. R. Raza and S. Atiq, *RSC Adv.*, 2025, **15**, 6308–6323.

53 L. Zeng, T. Wu, T. Ye, T. Mo, R. Qiao and G. Feng, *Nat Comput Sci.*, 2021, **1**, 725–731.

54 J. W. Gittins, Y. Chen, S. Arnold, V. Augustyn, A. Balducci, T. Brousse, E. Frackowiak, P. Gómez-Romero, A. Kanwade, L. Köps and P. K. Jha, *J. Power Sources*, 2023, **585**, 233637.
55 N. P. Ngidi, A. F. Koekemoer and S. S. Ndlela, *J. Energy Storage*, 2024, **89**, 111638.
56 G. Sriram, G. Hegde, K. Dhanabalan, Y. Kalegowda, D. Mouraliraman, R. S. Vishwanath, M. Kurkuri and T. H. Oh, *J. Energy Storage*, 2024, **94**, 112454.
57 F. Scarpioni, S. Khalid, R. Chukwu, N. Pianta, F. La Mantia and R. Ruffo, *ChemElectroChem*, 2023, **10**, e202201133.
58 A. C. Lazanas and M. I. Prodromidis, *ACS Meas. Sci. Au*, 2023, **3**, 162–193.
59 T. K. Shivasharma, R. Sahu, M. Thosare, D. Sarker, U. Deshpande and B. R. Sankapal, *Sci. Rep.*, 2025, **15**, 28406.
60 T. B. Deshmukh, A. Agarwal, A. C. Mendhe, M. Thosare and B. R. Sankapal, *Chem. Phys. Lett.*, 2025, **870**, 142070.
61 N. O. Laschuk, E. B. Easton and O. V. Zenkina, *RSC Adv.*, 2021, **11**, 27925–27936.
62 I. Beyers, A. Bensmann and R. H. Rauschenbach, *J. Energy Storage*, 2023, **73**, 109097.
63 A. Morag, X. Chu, M. Marczewski, J. Kunigkeit, C. Neumann, D. Sabaghi, G. Z. Zukowska, J. Du, X. Li, A. Turchanin, E. Brunner, X. Feng and M. Yu, *Angew. Chem., Int. Ed.*, 2024, **63**, 19.
64 G. C. Mohanty, C. C. Gowda, P. Gakhad, M. Sanjay, S. Sarkar, K. Biswas, A. Singh and C. S. Tiwary, *Mater. Adv.*, 2023, **4**, 3839–3852.
65 R. S. Karmur, D. Gogoi, S. Sharma, M. R. Das, A. Dalvi and N. N. Ghosh, *J. Mater. Chem. A*, 2024, **12**, 12762–12776.
66 C. Hu, B. Li, K. Nie, Z. Wang, Y. Zhang, L. Yi, X. Hao, H. Zhang, S. Chong, Z. Liu and W. Huang, *Angew. Chem., Int. Ed.*, 2024, **64**, 1.
67 F. Yu, T. Huang, P. Zhang, Y. Tao, F. Cui, Q. Xie, S. Yao and F. Wang, *J. Energy Storage*, 2019, **22**, 235–255.
68 B. A. Ali, O. I. Metwalli, A. S. G. Khalil and N. K. Allam, *ACS Omega*, 2018, **3**, 16301–16308.
69 P. V. Shinde, N. M. Shinde, J. M. Yun, R. S. Mane and K. H. Kim, *ACS Omega*, 2019, **4**, 11093–11102.
70 K. Nakahara, K. Oyaizu and H. Nishide, *Chem. Lett.*, 2011, **40**, 222–227.
71 Y. Liang, Z. Tao and J. Chen, *Adv. Energy Mater.*, 2012, **2**, 742–769.
72 M. Armand, S. Grugeon, H. Vezin, S. Laruelle, P. Ribiere, P. Poizot and J.-M. Tarascon, *Nat. Mater.*, 2009, **8**, 120–125.
73 Y. Morita, S. Nishida, T. Murata, M. Moriguchi, A. Ueda, M. Satoh, K. Arifuku, K. Sato and T. Takui, *Nat. Mater.*, 2011, **10**, 947–951.
74 Z. Li, S. Li, S. Liu, K. Huang, D. Fang, F. Wang and S. Peng, *Electrochem. Solid-State Lett.*, 2011, **14**, A171–A173.
75 F. R. Brushett, J. T. Vaughey and A. N. Jansen, *Adv. Energy Mater.*, 2012, **2**, 1390–1396.
76 S. Muench, A. Wild, C. Friebe, B. Häupler, T. Janoschka and U. S. Schubert, *Chem. Rev.*, 2016, **116**, 9438–9484.
77 D. R. Nevers, F. R. Brushett and D. R. Wheeler, *J. Power Sources*, 2017, **352**, 226–244.
78 C. Buhrmester, L. M. Moshurchak, R. L. Wang and J. R. Dahn, *J. Electrochem. Soc.*, 2006, **153**, A1800–A1804.
79 S. J. Visco, C. C. Mailhe, L. C. De Jonghe and M. B. Armand, *J. Electrochem. Soc.*, 1989, **136**, 661–664.
80 S. J. Visco, M. Liu and L. C. De Jonghe, *J. Electrochem. Soc.*, 1990, **137**, 1191–1192.
81 S. Nishida, Y. Yamamoto, T. Takui and Y. Morita, *ChemSusChem*, 2013, **6**, 794–797.
82 S. Tobishima and A. Yamaji, *Jpn. Kokai Tokkyo Koho*, 1982.
83 Y. Hanyu and I. Honma, *Sci. Rep.*, 2012, **49**, 453.
84 Z. Song, H. Zhan and Y. Zhou, *Chem. Commun.*, 2009, **448**.
85 T. B. Schon, B. T. McAllister, P.-F. Li and D. S. Seferos, *Chem. Soc. Rev.*, 2016, **45**, 6345–6404.
86 S. Sharma and P. Chand, *Results Chem.*, 2023, **5**, 100885.
87 J. Wang, S. Dong, B. Ding, Y. Wang, X. Hao, H. Dou, Y. Xia and X. Zhang, *Natl. Sci. Rev.*, 2017, **4**, 71–90.
88 S. Sagadevan, A. R. Marlinda, M. R. Johan, A. Umar, H. Fouad, O. Y. Alothman, U. Khaled, M. S. Akhtar and M. M. Shahid, *J. Colloid Interface Sci.*, 2019, **558**, 68–77.
89 (*a*) CCDC 2408554: Experimental Crystal Structure Determination, 2026, DOI: 10.5517/ccdc.csd.cc2lv992; (*b*) CCDC 2412264: Experimental Crystal Structure Determination, 2026, DOI: 10.5517/ccdc.csd.cc2lz4zq; (*c*) CCDC 2495748: Experimental Crystal Structure Determination, 2026, DOI: 10.5517/ccdc.csd.cc2ps10k.